Progress in Nuclear Energy 195 (2026) 106319

Contents lists available at ScienceDirect

Progress in Nuclear Energy

journal homepage: www.elsevier.com/locate/pnucene

Multi-objective topology optimization of heat pipe cooled reactor core subjected to thermo-mechanical loadings

Hao Jin [a], Mingkai Yue [b], Di Yun [c], Jinxiong Zhou [b],*

[a] School of Mechanical Engineering, Hangzhou Dianzi University, Hangzhou 310018, People's Republic of China
[b] State Key Laboratory for Strength and Vibration of Mechanical Structures and School of Aerospace, Xi'an Jiaotong University, Xi'an 710049, People's Republic of China
[c] Department of Nuclear Science and Technology, Xi'an Jiaotong University, Xi'an, 710049, People's Republic of China

ARTICLE INFO

Keywords:
Heat pipe cooled reactor
Multi-objective topology optimization
Thermal–mechanical coupling
Finite element analysis
Lightweight design

ABSTRACT

The Heat Pipe Cooled Reactor (HPR) is a critical component for mobile energy supply in extreme environments, such as deep space exploration, deep-sea submersion, and remote engineering operations, where lightweight design is a key performance indicator. Existing studies primarily focus on the layout and sizing of the heat pipes, while the matrix, which serves as both the primary heat transfer medium and the load-bearing structure, constitutes a significant portion of the mass but has not been adequately explored. The main challenge lies in balancing structural stiffness, thermal conductivity efficiency, and lightweight design. In this study, a thermal–mechanical coupling finite element model of solid-state core in the HPR is first established, considering the complex mechanical behaviors such as thermal expansion, creep, and gap heat transfer. Based on this, a multi-objective topology optimization framework is developed by combining Bi-directional Evolutionary Structural Optimization (BESO) theory with compromise programming, aiming to simultaneously minimize mechanical compliance and thermal compliance under a given volume constraint. The results demonstrate that the framework significantly reduces the mass of the matrix while maintaining thermal performance and structural stiffness. Additionally, the weight ratio factor adjustment feature of the optimization framework enables the construction of Pareto fronts, revealing the trade-off mechanism between heat dissipation performance and structural stiffness, thus providing multiple optimization solutions for practical engineering design decisions.

1. Introduction

Heat pipe-cooled reactors (HPRs) utilize an arrangement where fuel rods and heat pipes are intercalated within a solid-state matrix. The capillary force and phase-change characteristics of the heat pipes facilitate the efficient transfer of fission heat. This design eliminates the need for conventional reactor components such as circulation pumps and main pipelines, which are common in traditional liquid-cooled reactors. Consequently, the energy supply system exhibits key advantages, including passive safety, compact size, and simplified structure (Yan et al., 2020). As a result, HPRs hold substantial potential for future development and widespread applications in fields such as deep space exploration, deep-sea submersible operations, and mobile power supply for remote regions. Notable projects like NASA Kilopower and the Los Alamos National Laboratory HOMER project have validated the feasibility of kilowatt-level HPRs for planetary surface missions (Poston et al., 2020; Zhang et al., 2020). For megawatt-scale power requirements, designs like MegaPower present reliable solutions (Zhang et al., 2020). Additionally, the NUSTER series has expanded the use of HPRs to deep-sea applications (Peng et al., 2025).

Mastering thermal–mechanical coupling analysis methods is essential for structural optimization and performance evaluation. However, several factors significantly increase the complexity of this problem. Firstly, the thermal expansions of the heat pipes, fuel rods, and cladding in HPRs are interconnected, leading to complex, synergistic deformations within the reactor core (Cao and Wang, 2019; Jeong et al., 2023). Secondly, the assembly gaps between components introduce additional thermal resistance to the solid-state core, and the heat transfer mechanism is influenced by multiple factors (Cao and Wang, 2019; Sun et al., 2020). These gaps dynamically evolve with the thermal expansion and long-term creep of the components, potentially resulting in contact or closure (Ma et al., 2021). If the initial gap is too large, the surfaces may not make sufficient contact at steady state, causing heat transfer to primarily rely on less efficient radiation (Cao and Wang, 2019). Furthermore, the use of conductive inert gases, liquid metals, or other solid fillers to reduce gap thermal resistance adds complexity, as their

---

* Corresponding author.
E-mail address: jxzhouxx@mail.xjtu.edu.cn (J. Zhou).

https://doi.org/10.1016/j.pnucene.2026.106319
Received 27 July 2025; Received in revised form 18 January 2026; Accepted 21 February 2026

physical and chemical properties, dynamic gap evolution, and heat transfer behavior need to be accurately characterized. These factors make it difficult to predict the stress distribution and heat transfer paths in solid-state HPRs with precision, presenting significant challenges for core safety analysis and design optimization (Ma et al., 2021).

Due to these challenges, high-fidelity multiphysics numerical models have become essential tools for analyzing the thermal–mechanical coupling behavior of HPRs. Currently, the finite element method (FEM) is widely used to model such complex problems. Many studies, for instance, achieve a balance between numerical cost and accuracy by using commercial finite element software such as ABAQUS, ANSYS, or COMSOL Multiphysics to model the mesh structure of the fan-shaped region of the HPR core (ranging from one-quarter to one-twelfth of the core) (Ma et al., 2021; Sun et al., 2020). Researchers develop coupled thermodynamic models that account for heat conduction, material properties (such as creep, thermal expansion, irradiation effects, fuel burnup, fission gas release, and fuel relocation for stainless steel and uranium dioxide fuels), and gap heat transfer. These models enable the quantification of the maximum deformation, stress distribution, and temperature variation within the matrix. After validation with off-reactor experimental data or existing fuel performance tests, these models can accurately predict system behavior under various conditions, including long-term operation, transient states, and single heat pipe failure (Cao and Wang, 2019; Peng et al., 2025).

The HPR system offers the advantages of compactness and lightweight design, with lightweight optimization being a primary research focus for its role as a mobile energy supply device in various extreme environments. In the reactor core, uranium–molybdenum alloy is typically used to fabricate fuel rods, optimizing the enrichment distribution. The heat pipe layout is also adjusted to ensure power output while minimizing the core size and weight as much as possible (Sun et al., 2020; Zhang et al., 2020). For example, the Kilopower project successfully kept the total system mass under 400 kg while achieving a 15-year design life (Poston et al., 2020). The heat exchanger is the largest external mass component of the HPR core, and existing studies have proposed integrated material-structure design solutions to balance heat transfer efficiency with structural light weighting. For instance, lightweight, high-strength, and high thermal conductivity materials such as cesium–titanium and highly oriented pyrolytic graphite have been employed to fabricate thin-walled (0.1 to 0.2 mm) heat pipes and cooling fins (El-Genk and Schriener, 2025). Moreover, an efficient optimization framework has been developed by integrating surrogate models with genetic algorithms to optimize the layout of condenser pipes in the heat exchanger. This framework achieves precise temperature control and reduces the heat exchanger mass by 5.56% (Zhang et al., 2024).

The matrix is the largest structural component by mass in the solid-state reactor core, and there has been limited research specifically focused on its lightweight design. In HPRs, the matrix is a homogeneous continuous body containing fixed positions and numbers of holes (for fuel rods and heat pipes) that support both heat conduction and structural functions. It must ensure efficient heat transfer from the fuel rods to the heat pipes, while also protecting the heat pipes and fuel rods from mechanical damage due to vibrations and shocks. Therefore, the primary challenge in matrix lightweight design is balancing mass, heat transfer efficiency, and structural stiffness. The continuum-based multi-objective topology optimization method has demonstrated unique advantages for such problems. For instance, Sandilya Kambampati et al. using level-set topology optimization theory and Lagrange equations, integrated stiffness, thermal stress, and temperature response into a single expression, and derived sensitivities using the adjoint method to guide the addition or removal of elements. This method was applied to multi-objective topology optimization for fighter jet battery pack brackets, revealing that stress, stiffness, and temperature requirements typically conflict under volume constraints (Kambampati et al., 2020a). Ling et al. developed a multidisciplinary collaborative optimization platform for perforated plates in nuclear reactors, first conducting topology optimization for individual disciplines (such as static stiffness, natural frequency, and flow velocity) using relative element density as a shared variable. Through consistency equations, the system and disciplinary variables were iteratively linked to achieve optimized results (Ling et al., 2023). However, the repeated transfer of design variables across different layers can lead to inefficient convergence (Luo et al., 2021).

Compromise programming is a core concept of multi-objective topology optimization. It transforms multiple conflicting objectives into a single objective function through normalized weighted sums, aiming to bring the overall objective as close as possible to the optimal values of the individual sub-objectives (the ideal point or utopia point). This method effectively addresses disparities in dimensions and numerical values and allows for flexible adjustment of sub-objective weights, providing a comprehensive set of non-dominated solutions (the Pareto front) and offering a variety of design solutions (Hao et al., 2025). For example, Shi et al. first proposed a thermal-elasticity topology optimization formula, which, combined with additive manufacturing technology, successfully achieved over 18% weight reduction and performance enhancement, effectively addressing the combined mechanical and thermal loads (Guanghui et al., 2020). In the design of underwater vehicles (AUVs) and electric vehicle battery racks, Mao and Yan applied a thermal stress coupling topology optimization method, using element birth–death and weighted coefficient methods to simultaneously reduce structural mass, ensure stiffness, and control temperature gradients, ensuring proper battery pack operation (Mao and Yan, 2018; Huang et al., 2025). Additionally, Al Ali and Shimoda focused on multiphysics multi-scale collaborative topology optimization, aiming to optimize both macro and micro structures to design porous structures with lightweight, high thermal conductivity, and high stiffness, maximizing thermal conductivity and stiffness through normalized multi-objective functions (Ali and Shimoda, 2022). However, compared to thermal-elasticity body topology optimization with fixed hole positions, HPRs must consider the coupling effects of assembly gaps, heat pipes, fuel rods, and cladding on the matrix, making multi-objective topology optimization under thermal–mechanical coupling a new challenge for the matrix.

This study, based on Ross–Stoute gap heat transfer theory (Van Uffelen et al., 2019), fully considers real mechanical behaviors such as creep and swelling of materials in the solid-state reactor core under high-temperature irradiation conditions. By further developing the GAPCON and CREEP subroutines, a two-dimensional thermal–mechanical coupling numerical model for solid-state reactor cores suitable for ABAQUS was established. Additionally, a thermal–mechanical coupling multi-objective topology optimization program was developed for ABAQUS, based on BESO framework. This method successfully minimizes heat dissipation weakness and compliance under different volume fraction constraints and has been applied to the lightweight design of the solid-state reactor core matrix.

2. Coupled thermal–mechanical model

This study focuses on the classic hexagonal honeycomb layout of HPRs. To better illustrate the topology optimization problem of the matrix, the spacing between the holes is deliberately enlarged. The solid-state reactor core consists of 64 heat pipes and 96 fuel rods, with the specific geometric and material parameters of the components provided in Table 1. The thermal–mechanical coupling behavior of the HPR is shown in Fig. 1. During operation, the fission reaction in UO2 causes thermal expansion, swelling, and creep of the fuel rods. The generated heat is transferred through the assembly gaps, cladding, and matrix to the heat pipes, where the heat transfer medium within the pipes facilitates energy transfer. In this process, both the cladding and matrix primarily experience thermal expansion and creep, altering the gap size, which impacts heat transfer and may even result in contact between different components.

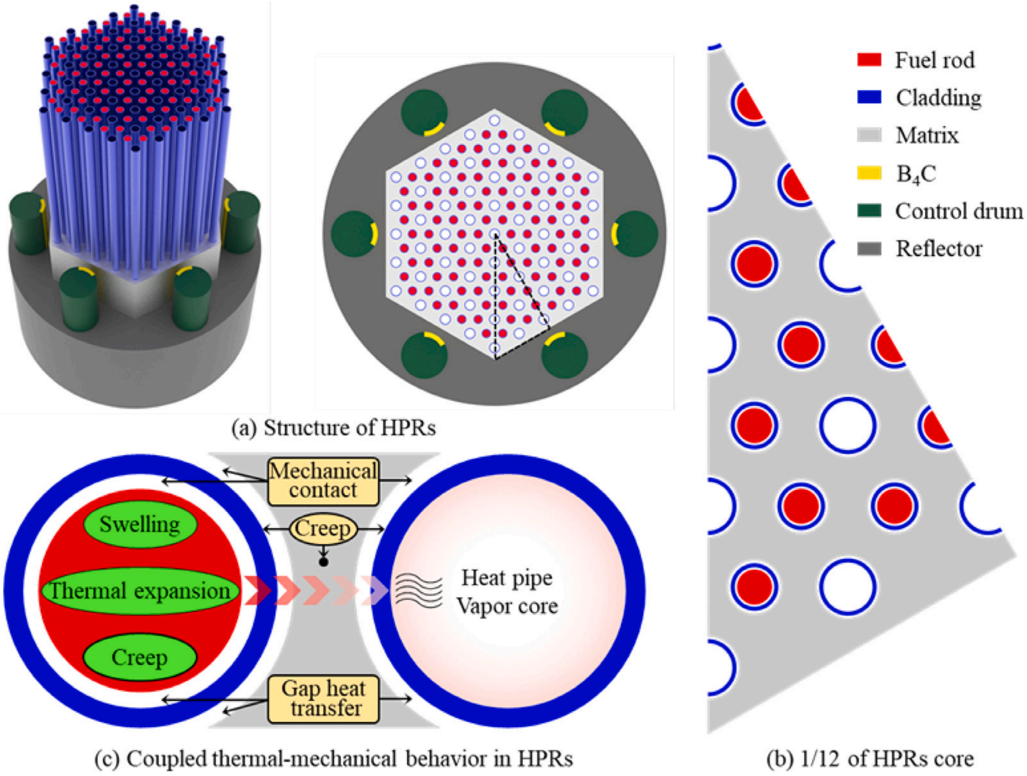

(a) Structure of HPRs

(c) Coupled thermal-mechanical behavior in HPRs

(b) 1/12 of HPRs core

Fig. 1. Structure diagram and heat transfer mechanisms of the solid-state core of HPR.

Table 1
Geometric parameters and materials of HPR.

Parameters	Value	Parameters	Value
Fuel material	UO_2	Cladding, Matrix	316SS
Fuel hole diameter (mm)	12	Core active length (mm)	1500
Heat pipe hole diameter (mm)	14	Total thermal power (kW)	500
Fuel-to-fuel distance (mm)	21	Operational life (a)	5
Fuel-to-Heat pipe distance (mm)	21	Heat Pipe Operating Temperature (°C)	675
Cladding thickness (mm)	1	Core Power Density (W/cm^3)	10
Gap (mm)	0.1	UO_2 Density (t/m^3)	10.52

2.1. Heat transfer model of structures with gas gaps

The primary mode of heat transfer in HPRs is solid heat conduction, which is governed by the Fourier heat conduction equation:

$$k\nabla^2 T + Q = \rho c \frac{\partial T}{\partial t} \tag{1}$$

where k is the thermal conductivity, T is the temperature, Q is the heat source power density, ρ is the density, c is the specific heat capacity, and t is time.

The gap heat transfer mechanism proposed by Ross and Stoute suggests that the heat transferred across the gap surface is determined by the surface temperatures and the equivalent gap heat transfer coefficient (Van Uffelen et al., 2019). The gap heat transfer model is given by:

$$q_g = h_{gap}\left(T_1 - T_2\right) \tag{2}$$

where q_g represents the gap heat flux, h_{gap} is the gap heat transfer coefficient, and T_1 and T_2 are the temperatures of the gap surfaces. The coefficient h_{gap} is determined by the heat transfer mechanisms within the gap and consists of three main components:

$$h_{gap} = h_g + h_s + h_r \tag{3}$$

where h_g is the gas heat transfer coefficient, h_s is the heat transfer coefficient between the gap surfaces contacted, and h_r is the radiation heat transfer coefficient between the gap surfaces.

2.1.1. Gap gas model

The value of h_g depends on the gap size and the roughness of the two surfaces. The gas temperature near the gap surface is not equal to the temperature of the solid surface, which is known as the temperature jump phenomenon. The roughness of the gap surfaces also plays a crucial role in determining the thermal conductivity of the gas in the gap. The gas heat transfer coefficient calculation model (Van Uffelen et al., 2019) is given by:

$$h_g = \frac{k_g}{d + C_r\left(R_1 + R_2\right) + g_1 + g_2} \tag{4}$$

where k_g is the thermal conductivity of the gas, d is the gap width, C_r is the roughness coefficient, R_1 and R_2 are the roughness values of the gap surfaces, and g_1 and g_2 are the temperature jump distances at the gap surfaces.

The calculation of the temperature jump distances is derived from the Kennard model (Kauzmann, 2012), and is expressed as:

$$g_1 + g_2 = 5756\frac{2 - a_{\mathrm{mix}}}{a_{\mathrm{mix}}}\frac{k_{\mathrm{mix}}\sqrt{T_{\mathrm{mix}}}}{p}\left(\sum_{i=1}^{n}\frac{X_i}{M_i}\right)^{\frac{1}{2}} \tag{5}$$

where a_{mix} is the mixture gas component adjustment factor, T_{mix} is the average temperature of the mixture gas, p is the pressure of the mixture gas, n is the number of gas species in the mixture, X_i is the molecular fraction of the ith gas, and M_i is the molecular weight of the ith gas.

In the gap gas heat transfer model, the gas is treated as a non-flowing solid for analysis, and the potential effects of convection heat transfer, which may arise from flow under heating conditions, are neglected. The thermal conductivity of the gas varies with temperature, gas composition, and reactor operating conditions. For instance, for a gas mixture consisting of He, Xe, and Kr, the thermal conductivity is calculated using the following expression:

$$k_g = \left(k_{\mathrm{He}}\right)^{\alpha}\left(k_{\mathrm{Xe}}\right)^{\beta}\left(k_{\mathrm{Kr}}\right)^{\gamma} \tag{6}$$

where α, β, and γ are the mole fractions of the respective gases.

2.1.2. Gap contact model

When local contact occurs at the gap surface, the contact area plays a crucial role in gap heat transfer. Due to the non-ideal smoothness of the contact surfaces, which possess a certain degree of surface roughness, only a portion of the contact area is actually in contact under compression, leaving a gap between the surfaces. Therefore, existing contact heat transfer models assume that the thermal conductivity coefficient is related to the contact pressure (Was et al., 2019):

$$h_{\mathrm{s}} = C_{\mathrm{s}}\frac{2k_1k_2}{k_1 + k_2}\frac{p_{\mathrm{c}}}{\delta^{1/2}H} \tag{7}$$

where C_{s} is the contact constant, typically determined through experiments, k_1 and k_2 are the thermal conductivities of the materials at the two contact surfaces, p_{c} is the contact pressure, $\delta = \left(0.5R_1^2 + 0.5R_2^2\right)^{1/2}$ is the average gas film thickness, and H is the Mohs hardness of the softer material in contact.

2.1.3. Radiative model

During gap heat transfer, radiation heat transfer plays an important role, particularly at higher temperatures. According to the Stefan–Boltzmann radiation heat transfer law (Van Uffelen et al., 2019):

$$h_r = \zeta F_{\mathrm{Rad}}\left(T_1^2 - T_2^2\right)\left(T_1 + T_2\right) \tag{8}$$

$$F_{\mathrm{Rad}} = \frac{1}{\frac{1}{\delta_1} + \frac{1}{\delta_2} - 1} \tag{9}$$

where ζ is the Stefan–Boltzmann constant, F_{Rad} is the radiation function that depends on the emissivities of the two surfaces, and δ_1 and δ_2 are the radiation emissivities of the gap surfaces. The specific values for the required gap heat transfer model parameters are obtained from the literature (Williamson, 2011).

2.2. Material creep model

Reactor component materials, due to prolonged exposure to high temperatures and radiation conditions, experience deformation caused by various factors, including elastic deformation, thermal expansion, creep, and potential swelling induced by fission products, among others (Was et al., 2019; Holmström et al., 2013; Liu et al., 2020; Gilbert and Garner, 2007; Yvon and Carré, 2009; Gaffard et al., 2005). The total material strain rate is:

$$\dot{\varepsilon}_{\mathrm{totlp}} = \dot{\varepsilon}_{\mathrm{ep}} + \dot{\varepsilon}_{\mathrm{qp}} + \dot{\varepsilon}_{\mathrm{cp}} + \dot{\varepsilon}_{\mathrm{sw}} \tag{10}$$

In this context, $\dot{\varepsilon}_{\mathrm{totlp}}$ represents the total strain rate, $\dot{\varepsilon}_{\mathrm{ep}}$ is the elastic strain rate, $\dot{\varepsilon}_{\mathrm{tp}}$ is the thermal expansion strain rate, $\dot{\varepsilon}_{\mathrm{cp}}$ is the creep strain rate, and $\dot{\varepsilon}_{\mathrm{sw}}$ is the swelling strain rate.

According to the MATPRO fcreep material model, the creep strain rate $\dot{\varepsilon}_{\mathrm{cp}}^{\mathrm{UO_2}}$ for UO2 fuel pellets is given by:

$$\dot{\varepsilon}_{\mathrm{cp}}^{\mathrm{UO_2}} = \frac{\left(A_1 + A_2F_{\mathrm{r}}\right)\sigma_{\mathrm{e}}\mathrm{e}^{-\frac{Q_1}{RT}}}{\left(A_3 + D\right)G^2} + \frac{\left(A_4 + A_8F_{\mathrm{r}}\right)\sigma_{\mathrm{e}}^{4.5}\mathrm{e}^{-\frac{Q_2}{RT}}}{A_6 + D} + A_7F_{\mathrm{r}}\sigma_{\mathrm{e}}\mathrm{e}^{-\frac{Q_3}{RT}} \tag{11}$$

where F_{r} is the burnup rate, σ_{e} is the equivalent Mises stress, R is the ideal gas constant, D is the percentage fuel density, G is the average grain size, and A_i are material constants. Q_i represents the activation energy for the material, with specific values from Macdonald and Thompson (1976).

According to the MATPRO swelling material model, the total swelling $\varepsilon_{\mathrm{sw}}^{\mathrm{UO_2}}$ of the UO2 fuel pellet is the sum of the solid fission swelling $\varepsilon_{\mathrm{sws}}^{\mathrm{UO_2}}$ and the gas fission swelling $\varepsilon_{\mathrm{swg}}^{\mathrm{UO_2}}$, where:

$$\varepsilon_{\mathrm{sws}}^{\mathrm{UO_2}} = 2.5\times10^{-29}F_{\mathrm{r}} \tag{12}$$

$$\varepsilon_{\mathrm{swg}}^{\mathrm{UO_2}} = 8.8\times10^{-56}F_{\mathrm{r}}(2800 - T)^{11.73}\mathrm{e}^{-0.0162(2800-T)-8.0\times10^{-27}F_{\mathrm{r}}} \tag{13}$$

For the cladding and matrix made from 316SS, which do not undergo fission reactions, only creep behavior is considered. The creep strain rate model for 316SS is as follows:

$$\dot{\varepsilon}_{\mathrm{cp}}^{316\ \mathrm{L}} = \frac{C_1C_2\sigma_{\mathrm{e}}}{\sqrt{2C_2t + C_2^2t^2}} + mC_3\left(\frac{2\sqrt{3}}{3}\right)^{n+1}\sigma_{\mathrm{e}}^{n}t^{m-1} + 2.5C_4\left(\frac{2\sqrt{3}}{3}\right)^{n+1}\sigma_{\mathrm{e}}^{n}t^{1.5} \tag{14}$$

where t is time, C_i, m, and n are empirical parameters, with specific values from Holmström et al. (2013).

2.3. Finite element model and coupling strategy

In this study, the 1/12 structure of the HPRs shown in Fig. 1(b) is selected as a representative unit cell of the full structure. The geometric parameters and material compositions of each component are listed in Table 1; time- and temperature-dependent material property parameters for 316SS and UO_2 are available via the hyperlink at the end of the manuscript. The creep behavior of these materials requires the development of an UMAT subroutine for implementation. The finite element model of the representative unit cell structure was created in the commercial finite element software ABAQUS 2020, using 4-node generalized plane strain elements (CPEG4T) for meshing. The average mesh size is 0.4 mm, and the total number of elements is 26542, with a mesh independence test conducted. To represent the thermal–mechanical coupled response of the complete HPR structure, the boundary conditions on the left and right sides of the representative unit cell are set as symmetric in the cylindrical coordinate system, while the bottom edge is free. For temperature boundary conditions, the inner edge surface of the cladding in the heat pipe is assigned a convective heat transfer coefficient of 10 mW/mm^2/K, and the fuel rod is assigned a body heat flux of 10 mW/mm^3. All other boundaries are set as adiabatic. An initial temperature of 948 K is uniformly applied to all components. The behavior of the gap is modeled using the contact module, with the mechanical contact properties defined as normal hard contact and frictionless tangential contact. The heat transfer properties are implemented through the additional GAPCON program. The Coupled Temp–Displacement (Transient) solver is used to solve the thermal–mechanical coupling problem of the HPRs, with a simulation period of 5 years, assuming small deformation behavior. The technical roadmap for the entire coupled thermal–mechanical model is shown in Fig. 2.

2.4. Model verification

To validate the correctness of the present coupled thermo-mechanical model, a simplified version of the classical UO_2–Zr

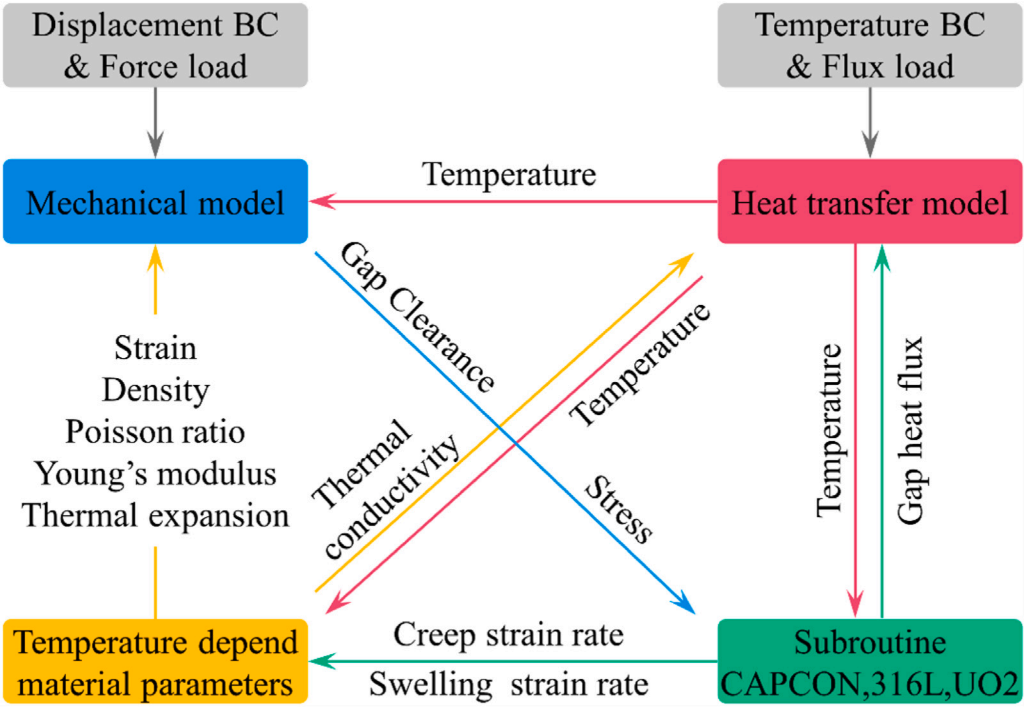

Fig. 2. Coupled thermal–mechanical model.

fuel rod–cladding gap heat-transfer benchmark is adopted. The computational conditions and model parameters are taken from Williamson et al. (2012). The fuel-rod radius is 4.1 mm, the axial length is 11.9 mm, and the initial gap width is 80 μm. A uniform convective boundary condition is imposed on the outer surface of the cladding to simulate coolant heat removal. The linear power increases linearly over 3 h and then remains constant for 3.2 years. Specifically, the average linear heat rate is 200 $W\cdot cm^{-1}$, the fast-neutron flux is 9.5×10^{17} $n\cdot m^{-2}\cdot s^{-1}$, the coolant pressure is 15.5 MPa, the coolant temperature is 530 K, the convective heat-transfer coefficient is 7500 $W\cdot m^{-2}\cdot K^{-1}$, the initial helium fill-gas pressure is 2 MPa, and the burnup at full fuel densification is 5 $MWd\cdot kgU^{-1}$. As a benchmark, this case has been used to validate fuel-performance codes for high-power-reactor fuel–deformation simulations, including BISON (Williamson et al., 2012), CAMPUS (Liu et al., 2016), and NECP-CALF (Liu et al., 2021). Recently, the same benchmark was again employed by Yang et al. to verify the correctness of a thermo-mechanically coupled solid-state reactor-core model developed on the COMSOL platform (Yang et al., 2025).

Based on the original case geometry and thermal–hydraulic parameters, we reconstructed the finite element model shown in Fig. 3(a) (a quarter-symmetric 2D model with 2026 generalized plane strain elements) using the strategy proposed in this work. The focus was to compare the gap evolution and the fuel rod centerline temperature evolution obtained from our model with those from the four reference models. As shown in Fig. 3(a), at the onset of power release, the fuel centerline temperature in all five models reached approximately 1300 K. With increasing burnup, the fuel centerline temperature in the four reference models exhibited an initial decrease followed by a slight rebound. As burnup further increased, the gap narrowed, resulting in a subsequent rise in fuel centerline temperature. In contrast, in our model (ABAQUS), prior to gap closure, the temperature level and trend were essentially consistent with those of the four models. However, as the gap narrowed and eventually closed, the fuel centerline temperature exhibited a decreasing trend. This deviation arises from the fact that our model neglects the influence of fuel burnup on thermal conductivity (Williamson, 2011).

Fig. 3(b) illustrates the evolution of the fuel–cladding gap with increasing burnup for the five models. Initially, all models demonstrated a phenomenon in which the gap decreased and then suddenly increased slightly (around 3.6 $MWd\cdot kgU^{-1}$, as shown in the displacement contour of Fig. 3(c)). This behavior indicates that the models successfully captured the densification process of the fuel pellets. Subsequently, the gap continued to decrease until eventual closure. Since the effect of fission gas release on the increase in plenum pressure was neglected, the gap in our model closed slightly faster compared with the four reference models. Fig. 3(c) presents the structural deformation, stress transfer, and temperature distribution associated with densification, initial gap closure, and post-closure conditions.

Although the material system of the HPR solid-state core (UO_2-316SS) differs from that of the benchmark (UO_2-Zr), the underlying finite element framework remains fundamental. The variation in materials manifests solely as updates to the constitutive model input parameters, while the governing thermo-mechanical equilibrium equations and the core numerical algorithms remain invariant. This consistency ensures the solver's applicability across different material systems.

Moreover, while the benchmark serves as a local model, it comprehensively captures the critical, strongly nonlinear physical processes inherent to the global HPR model. These include burnup-dependent fuel evolution encompassing thermal expansion, creep, swelling, and densification—as well as the complex contact mechanics and gap heat transfer at the fuel–cladding interface. The fidelity of this modeling strategy is substantiated not only by cross-validation with established codes but, more significantly, by recent out-of-pile scaled experiments on honeycomb matrices (Yang et al., 2025; Peng et al., 2025). Utilizing Digital Image Correlation (DIC) and infrared thermography, these experiments confirmed that the proposed numerical approach accurately predicts steady-state temperature fields, displacement distributions under single heat pipe failure, and long-term creep trends. This empirical evidence strongly supports the reliability of extending this strategy to the global 2D model (UO_2-316SS).

Crucially, despite the intricate lightweight configurations generated by topology optimization, the topological continuity of the matrix is

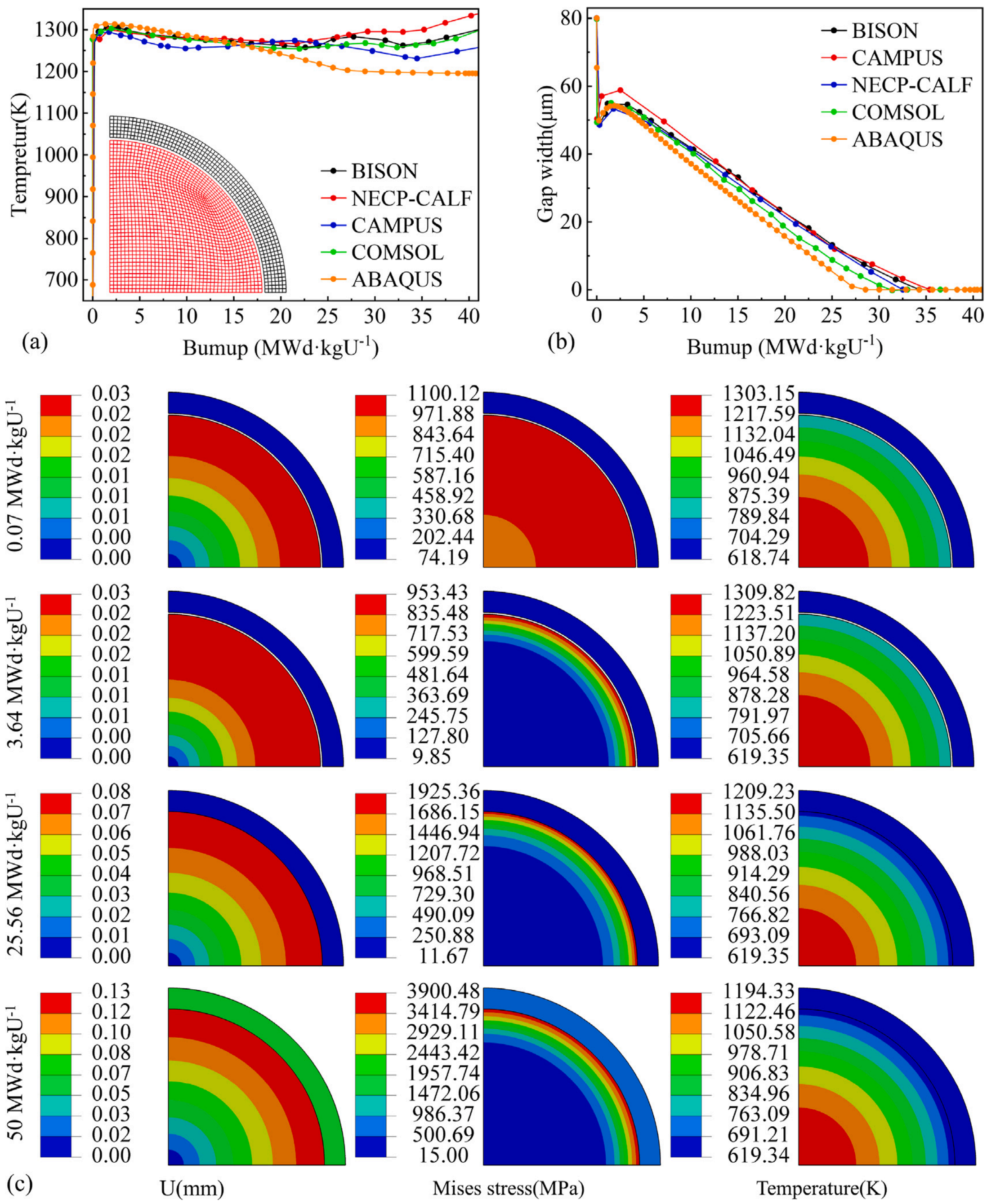

Fig. 3. Validation model and analysis results: (a) fuel centerline temperature vs. burnup. (b) Fuel–cladding gap width vs. burnup. (c) Distributions of structural displacement, Mises stress and temperature at representative burnup levels.

strictly preserved through regional constraints and algorithmic controls. This ensures that the physical mechanisms verified by the local model remain valid at the global level and that the initial equivalent thermo-mechanical boundary conditions are conserved. Consequently, the full-core simulations and topology optimization results derived from this framework are reliable.

3. Multi-objective topology optimization of solid-state reactor core

3.1. Optimization problem statement

This study considers a multi-objective optimization problem with two objective functions: mechanical compliance J_m and thermal compliance J_{th} . The first objective function aims to maximize the structural stiffness, minimizing deformation under mechanical loads. The second objective function seeks to maximize the thermal performance of the structure, minimizing the average temperature within the design domain. After normalizing these two independent objectives, they are combined into a single objective function through linear weighting, as shown in Eq. (15). By adjusting the weight factors (w_1 and w_2), the optimization results can balance the two objectives, thereby obtaining the Pareto front representing the set of optimal solutions for the multi-objective problem.

$$\begin{aligned}
&\min_{\mathbf{X}} : J = w_1 \frac{J_{\mathrm{m}} - J_{\mathrm{m}}^*}{J_{\mathrm{m}}^0 - J_{\mathrm{m}}^*} + w_2 \frac{J_{\mathrm{th}} - J_{\mathrm{th}}^*}{J_{\mathrm{th}}^0 - J_{\mathrm{th}}^*} \\
&\text{subject to: } \mathbf{X} = \left\{x_e\right\}, x_e = 1 \text{ or } x_{\min}, \forall e = 1, \ldots, N \\
&\qquad \mathbf{K}_{\mathrm{m}}\mathbf{U} = \mathbf{F}_{\mathrm{m}} \\
&\qquad \mathbf{K}_{\mathrm{th}}\mathbf{T} = \mathbf{Q} \\
&\qquad V(\mathbf{X}) = \sum_{e=1}^{N} x_e v_e = V^* \\
&\qquad w_1 + w_2 = 1
\end{aligned} \tag{15}$$

Here, x_e represents the relative density of the eth element (design variable), which can take the values of 1 (indicating the presence of solid material) or $x_{\min}$ (in this study, $x_{\min} = 0.001$, representing material removal). $\mathbf{X}$ is the vector of all design variables, and N denotes the total number of elements. $\mathbf{F}_{\mathrm{m}}$ is the global mechanical force vector, $\mathbf{U}$ is the global displacement vector, $\mathbf{K}_{\mathrm{m}}$ is the global mechanical stiffness matrix, $\mathbf{K}_{\mathrm{th}}$ is the global thermal conductivity stiffness matrix, $\mathbf{T}$ is the global nodal temperature vector, and $\mathbf{Q}$ is the global thermal load vector. V represents the total volume of the structure, v_e is the volume of the eth element, and V^* is the applied volume constraint value. The equation $\mathbf{K}_{\mathrm{m}}\mathbf{U} = \mathbf{F}_{\mathrm{m}}$ ensures the static equilibrium of the structure, while the equation $\mathbf{K}_{\mathrm{th}}\mathbf{T} = \mathbf{Q}$ governs the steady-state thermal equilibrium. In this study, these two equations are solved as independent cases with the same structure and boundary conditions. J_{m}^* and J_{th}^* represent the optimal solutions to the compliance-only and thermal compliance-only optimization problems, respectively, while J_{m}^0 and J_{th}^0 are the initial design values.

3.2. Sensitivity analysis

The detailed expressions for the two optimization sub-objectives are as follows:

$$\begin{aligned}
J_{\mathrm{m}}(\mathbf{X}) &= \mathbf{F}_{\mathrm{m}}^{\mathrm{T}}\mathbf{U} = \mathbf{U}^{\mathrm{T}}\mathbf{K}_{\mathrm{m}}\mathbf{U} = \sum_{e=1}^{N} \mathbf{u}_{\mathrm{e}}^{\mathrm{T}}\mathbf{k}_{\mathrm{m,e}}\mathbf{u}_{\mathrm{e}} \\
J_{\mathrm{th}}(\mathbf{X}) &= \mathbf{Q}^{\mathrm{T}}\mathbf{T} = \mathbf{T}^{\mathrm{T}}\mathbf{K}_{\mathrm{th}}\mathbf{T} = \sum^{N} \mathbf{t}_{\mathrm{e}}^{\mathrm{T}}\mathbf{k}_{\mathrm{th,e}}\mathbf{t}_{\mathrm{e}}
\end{aligned} \tag{16}$$

Where $\mathbf{u}_e$ is the displacement vector of the eth element node, and $\mathbf{k}_{\mathrm{m},e}$ is the element stiffness matrix; $\mathbf{t}_e$ is the temperature vector of the eth element node, and $\mathbf{k}_{\mathrm{th},\,e}$ is the element thermal conductivity stiffness matrix.

In the BESO theory, the equivalent stiffness matrix $\mathbf{k}_{\mathrm{m},e}$ and the equivalent thermal conductivity stiffness matrix $\mathbf{k}_{\mathrm{th},\,e}$ are linearly related to the design variables (Zuo and Xie, 2015; He and Liu, 2008):

$$\begin{aligned}
\mathbf{k}_{\mathrm{m,e}} &= x_e^p \mathbf{k}_{\mathrm{m}}^0 \\
\mathbf{k}_{\mathrm{th,e}} &= x_e^p \mathbf{k}_{\mathrm{th}}^0
\end{aligned} \tag{17}$$

Where p is the penalty exponent, and $\mathbf{k}_{\mathrm{m}}^0$ and $\mathbf{k}_{\mathrm{th}}^0$ are the initial element stiffness matrix and thermal conductivity stiffness matrix for the structure.

As a gradient-based method, the update of the design variables depends on the element sensitivities obtained by differentiating the objective function:

$$\begin{aligned}
\alpha_e^{\mathrm{m}} &= \frac{\partial J_{\mathrm{m}}(\mathbf{X})}{\partial x_e} = p x_e^p \mathbf{u}_{\mathrm{e}}^{\mathrm{T}}\mathbf{k}_{\mathrm{m,e}}\mathbf{u}_{\mathrm{e}} \\
\alpha_e^{\mathrm{th}} &= \frac{\partial J_{\mathrm{th}}(\mathbf{X})}{\partial x_e} = p x_e^p \mathbf{t}_{\mathrm{e}}^{\mathrm{T}}\mathbf{k}_{\mathrm{th,e}}\mathbf{t}_{\mathrm{e}}
\end{aligned} \tag{18}$$

It is important to note that $\mathbf{u}_{\mathrm{e}}^{\mathrm{T}}\mathbf{k}_{\mathrm{m},e}\mathbf{u}_{\mathrm{e}}$ represents the elastic strain energy of the element, and $\mathbf{k}_{\mathrm{th},e}\mathbf{t}_{\mathrm{e}}$ represents the vector of thermal flux composed of the thermal flux at all Gauss integration points of the element. These physical quantities can be directly extracted from the results of the finite element analysis.

By substituting Eqs. (16) and (17) into Eq. (18), the element sensitivity for the multiobjective topology optimization model is obtained:

$$\alpha_e = \frac{\partial J(\mathbf{X})}{\partial x_e} = \frac{w_1}{J_{\mathrm{m}}^0 - J_{\mathrm{m}}^*}\alpha_e^{\mathrm{m}} + \frac{w_2}{J_{\mathrm{th}}^0 - J_{\mathrm{th}}^*}\alpha_e^{\mathrm{th}} \tag{19}$$

3.3. Design variable update algorithm

To prevent mesh dependence and checkerboard patterns, the sensitivity values are first smoothed using a filtering scheme:

$$\hat{\alpha}_e = \frac{\sum_j^N w\left(r_{ej}\right)\alpha_j}{\sum_j^N w\left(r_{ej}\right)} = \sum_j^N \left(\frac{w\left(r_{ej}\right)}{\sum_j^N w\left(r_{ej}\right)}\alpha_j\right) = \sum_j^N \eta_j \alpha_j \tag{20}$$

$$w\left(r_{ej}\right) = \max\left(0, r_{\min} - r_{ej}\right) \tag{21}$$

Where r_{ej} is the distance between elements e and j, w is the weight function used to average the original sensitivity, and $r_{\min}$ is the filter radius. The weight factor η_j is independent of the sensitivity value and is computed prior to the start of the topology optimization process. The current sensitivity values (at the kth iteration) are averaged with the historical data from the previous design iteration (at the $(k-1)$th iteration) to improve convergence:

$$\tilde{\alpha}_e = \frac{\hat{\alpha}_e^k + \hat{\alpha}_e^{k-1}}{2} \tag{22}$$

BESO begins with a complete design and iteratively reduces the structural volume by switching the states of elements. In each iteration, the target volume V^{k+1} for the next iteration is determined based on the current volume V^k and an evolution rate ert:

$$V^{k+1} = V^k(1 - ert) \tag{23}$$

In order to efficiently add and remove material, BESO employs the bisection method to determine the sensitivity threshold, thereby enforcing the material volume fraction constraint in each iteration. The method involves sorting the sensitivity values of all elements in the current iteration and progressively approaching an appropriate threshold, ensuring that the updated material distribution meets the required target volume fraction. The detailed process is as follows:

→ Initialization: The upper and lower bounds of the sensitivity threshold are denoted as $\tilde{\alpha}_e^{\max}$ and $\tilde{\alpha}_e^{\min}$, corresponding to the maximum and minimum sensitivity values across all elements in the current design, respectively.

→ Computation: The candidate sensitivity threshold for the current iteration is computed as:

$$\tilde{\alpha}_{\mathrm{th}} = \frac{\tilde{\alpha}_e^{\max} + \tilde{\alpha}_e^{\min}}{2} \tag{24}$$

Elements are then classified according to the following rule:

- If $\tilde{\alpha}_e > \tilde{\alpha}_{\mathrm{th}}$, set $x_e = 1$.
- Otherwise, set $x_e = 0.001$.

→ Statistical Update: The material volume fraction of the updated structure is calculated as:

$$V = \frac{\sum_{e=1}^N x_e}{\sum_{e=1}^N w_e} \tag{25}$$

This value is then compared to the target volume fraction V^*:

- If $V > V^*$, it indicates that the current threshold is too low, and the lower bound should be updated to $\tilde{\alpha}_e^{\min} = \tilde{\alpha}_{\text{th}}$.
- If $V < V^*$, it indicates the threshold is too high, and the upper bound should be updated to $\tilde{\alpha}_e^{\max} = \tilde{\alpha}_{\text{th}}$.

→ Convergence Check: Steps 2–3 are repeated until the relative error between the upper and lower bounds satisfies the convergence condition:

$$\frac{\tilde{\alpha}_e^{\max} - \tilde{\alpha}_e^{\min}}{\tilde{\alpha}_e^{\max}} < \zeta \tag{26}$$

where ζ is the given convergence tolerance, set to 1×10^{-5} in this study.

The final threshold $\tilde{\alpha}_{\text{th}}$ will be applied in the current iteration to determine material addition and removal, ensuring precise control of material volume throughout the topology optimization process.

3.4. Topology optimization framework

The multi-objective topology optimization proposed in this study is implemented through the integration of ABAQUS 2020 with Python code. One notable contribution of this framework is the utilization of the convenient preprocessing and advanced solver technologies provided by commercial finite element software, which facilitates extending the proposed method to various design problems and optimization tasks. To ensure accessibility, we have made the program open-source. The execution flow of this framework is illustrated in Fig. 4.

First, two finite element models with identical geometry, material, and mesh information are created within the ABAQUS/CAE environment. One model is assigned mechanical loads and displacement boundary conditions, referred to as Load Case 1, while the other is assigned thermal loads and temperature boundary conditions, referred to as Load Case 2. After manually inputting the structural volume constraint and the minimum filtering radius, the topology optimization Python program is executed. Load Case 1 is solved using the General Static analysis step, and Load Case 2 is solved using the Heat Transfer analysis step, generating two result files with the odb extension.

The program processes each element's Gauss integration points and nodal physical quantities from both result files and applies Eqs. (16)–(18) to calculate the mechanical compliance and thermal compliance optimization objectives for each element's sensitivity. These sensitivity values are then multiplied by the specified weighting factors and input into Eq. (19) for linear weighted aggregation. After filtering and BESO optimization analysis, the updated design variable information is obtained, and the material distribution in both Load Case 1 and Load Case 2 models is updated. This process is repeated until the volume constraint and convergence criteria for the overall optimization goal (Eq. (27)) are satisfied, with m set to 5 in this study.

$$\epsilon = \frac{\left|\sum_{i=1}^{m}\left(J_{k-i+1}(\mathbf{X}) - J_{k-i+1-m}(\mathbf{X})\right)\right|}{\sum_{i=1}^{m} J_{k-i+1}(\mathbf{X})} \leq 0.001 \tag{27}$$

Additionally, this study explores the use of ABAQUS direct coupling analysis technique for thermal and mechanical physics fields, namely the Coupled Temp–Displacement analysis step, which allows the integration of the two independent finite element models. The physical quantities from the resulting single file are then extracted for sensitivity analysis and design variable updates, in line with the approach shown in Fig. 4. The final optimization results are consistent, simplifying the execution process.

Given that directly integrating the HPRs thermal–mechanical coupled finite element model with the multi-objective topology optimization program could lead to convergence issues and longer computational times, this study adopts the approach illustrated in Fig. 4. Initially, only a single matrix finite element model is used, and the full HPRs thermal–mechanical coupled model is simplified to derive the equivalent boundary conditions for the matrix. In this setup, the blue edge represents the symmetric displacement boundary condition in the cylindrical coordinate system, the red edge corresponds to the surface heat source derived from the full fuel rod power, the green edge represents the convective heat transfer boundary condition of the heat pipe, and the black edge represents the adiabatic boundary condition. To ensure the integrity of the heat pipe boundary, a 2 mm protective zone is maintained, and subsequent optimization is only performed on the dark gray area.

Additionally, the pressure on the heat pipe hole wall surface, the pressure on the fuel rod hole wall surface, and the surface heat source are extracted from the complete thermal–mechanical coupled finite element model analysis. These values are then applied to the edges of the circular hole in the matrix of the simplified model to achieve stress and temperature distributions that are consistent with those from the full model. Subsequently, the optimized matrix geometry is reassembled with the heat pipe shell, fuel rod shell, and fuel rod. The complete HPRs thermal–mechanical coupled finite element model is re-established for numerical simulations, enabling the accurate analysis of the effects of the new matrix configuration on the overall structural stress, temperature, heat transfer efficiency, and stiffness.

4. Optimization results

4.1. L-bracket

This study uses the classic L-bracket structure as a benchmark to validate the topology optimization method. As shown in Fig. 5, the L-bracket is derived by removing a 60 mm × 60 mm section from the top-right corner of a 100 mm square with a thickness of 1 mm. The Young's modulus is 120 GPa, Poisson's ratio is 0.3, the thermal expansion coefficient is $8.6 \times 10^{-6}/°\text{C}$, and thermal conductivity is $0.02\ \text{W/mm}\cdot\text{K}$. A concentrated heat source of 1.38 W and a mechanical force of 5000 N are applied to the right endpoint, while the left top endpoint is fixed, and a 20 K temperature field is uniformly applied to the remaining areas. The structure is discretized using 1 mm plane four-node elements, and a steady-state Coupled temp–displacement analysis is performed. The volume fraction for topology optimization is set to 50%, with a minimum filter radius of 5 and an evolution rate of 0.02.

Fig. 5 shows the optimization results for the L-bracket, with mechanical compliance (J_m) and thermal compliance (J_{th}) as objectives. In Fig. 5(a), the Pareto front is presented for varying thermal compliance weights (w_1) between 0 and 1. As w_1 increases, mechanical compliance rises from 18.04 J to about 43.38 J, while thermal compliance decreases from 3.22 to 1.15 $\text{MW}\cdot\text{K/mm}$, demonstrating a clear trade-off between the two objectives. This reveals that the proposed compromise programming framework effectively captures the trade-offs in the design space.

Fig. 5(b) further illustrates the optimization iteration process with a compromise weight of $w_1 = 0.5$. The global objective function J and volume constraint V stabilize and converge within 40 iterations. The topology evolution shows the material layout evolving from an initial density field to a clear skeletal structure, with smooth boundaries, validating the stability and manufacturability of the optimization algorithm.

To assess the sensitivity of the optimization results to objective weights, Fig. 5(c) shows the trends in maximum temperature, displacement, and Mises stress for different weight combinations. As the thermal compliance weight increases, the maximum temperature significantly drops from 636.96 K to 427.35 K, while the maximum displacement rises from 6.73 mm to 17.78 mm, and maximum stress increases from 5.37 GPa to 14.76 GPa. This indicates that improving heat dissipation requires a trade-off in structural stiffness and strength.

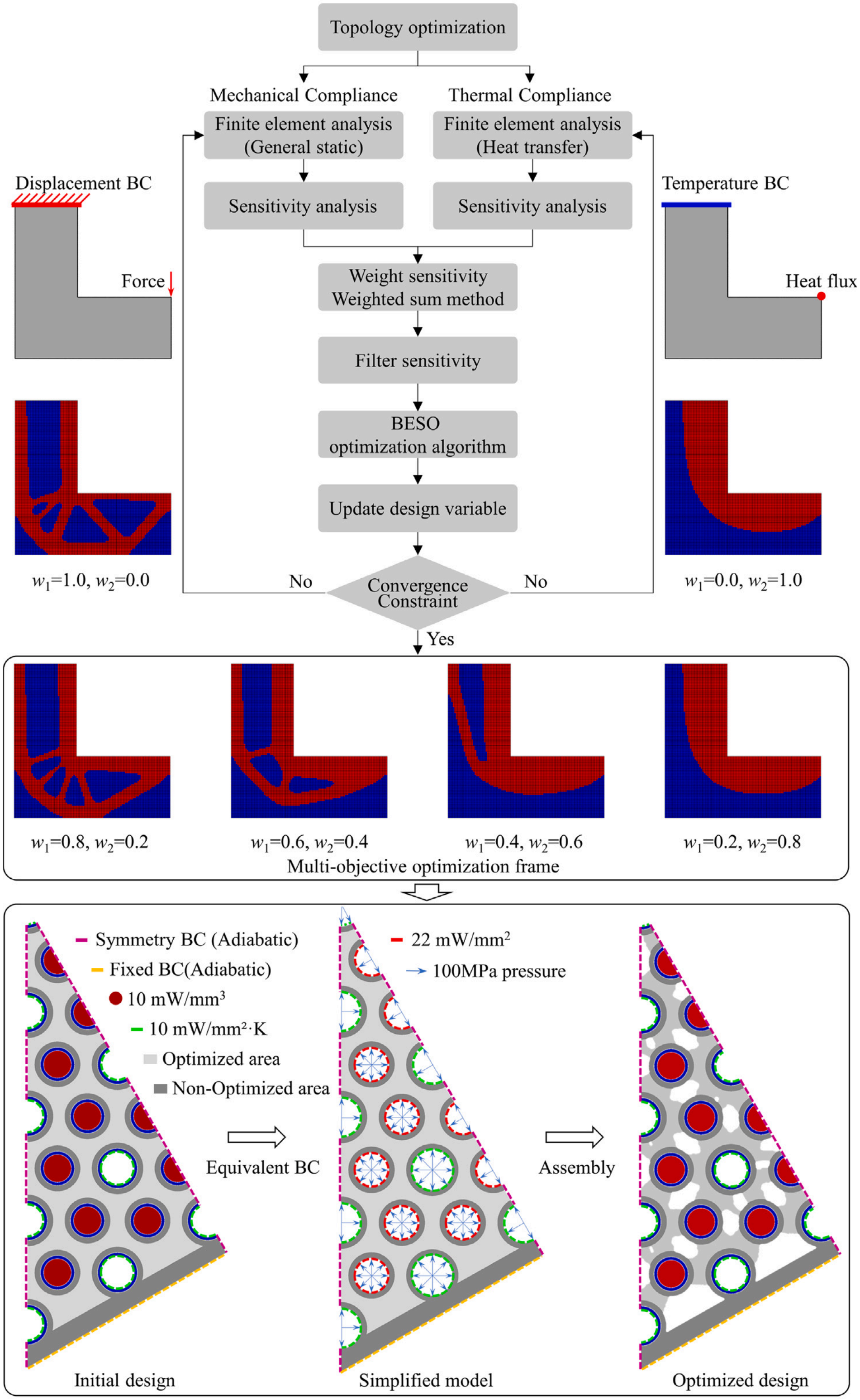

Fig. 4. Multi-objective topology optimization framework for the HPR matrix.

Fig. 5(d) presents displacement, temperature, and stress field contours for three typical designs: pure mechanical ($w_1 = 0$), compromise ($w_1 = 0.5$), and pure thermal ($w_1 = 1$). The pure mechanical design maintains thick ribs, with low displacement and stress but significant internal heat accumulation. The pure thermal design strengthens the

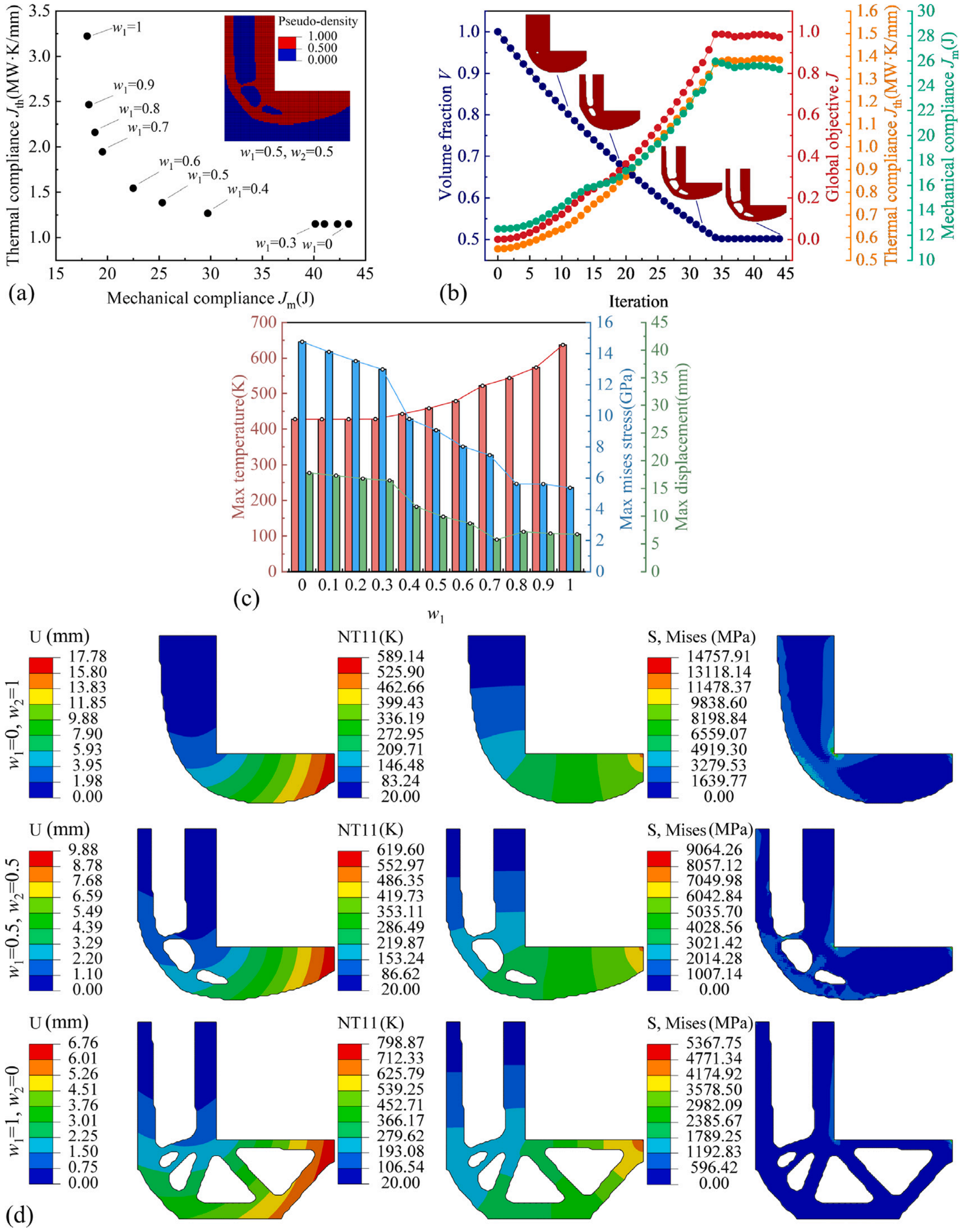

Fig. 5. L-bracket thermal–mechanical coupling topology optimization: (a) Pareto front. (b) Iteration process of optimization objectives and constraint functions. (c) Optimization results of maximum temperature, maximum stress, and maximum displacement under different weight factors. (d) FEA results of three typical optimal designs.

heat conduction path, improving thermal performance, but significantly reduces structural stiffness and increases stress concentration. The compromise design, with balanced ribs and hole layouts, achieves a good balance between structural and thermal performance, with temperature, displacement, and stress levels falling within an optimal range. This example validates the correctness of the multi-objective optimization approach and the algorithm, providing a set of Pareto solutions for practical engineering design selection.

4.2. Solid-state core of HPRs

4.2.1. Initial design

Fig. 6 presents the key physical quantity contours of the initial HPR design after five years, based on the thermal–mechanical coupling finite element analysis method proposed in this study. The temperature distribution of the entire solid-core reactor ranges from 948.82 K to 988.64 K, showing a gradient decline from the center to the periphery (Fig. 6(a)). The enlarged view of 1/6 of the matrix shows the

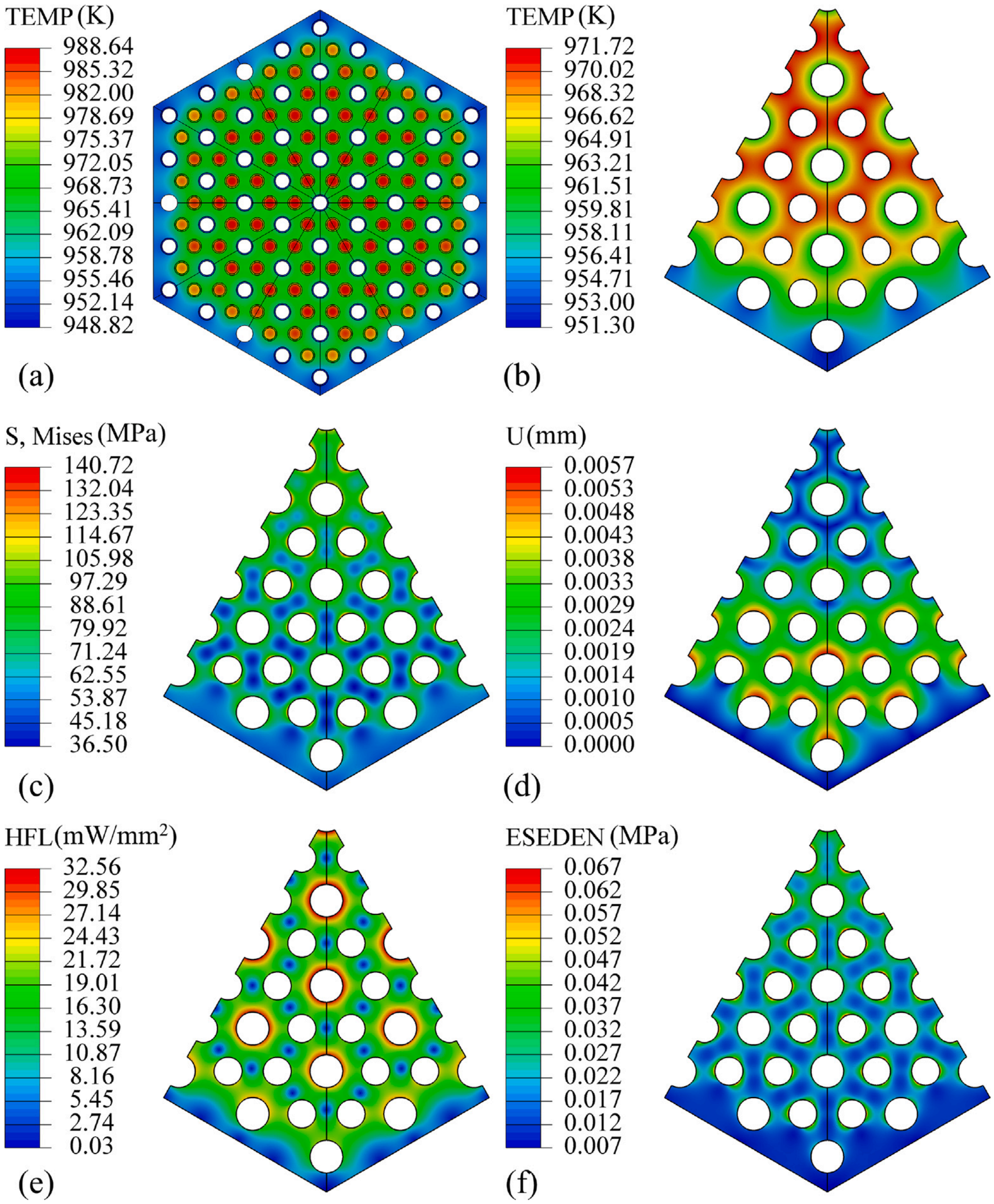

Fig. 6. Thermal–mechanical analysis of the HPR initial design: (a) assembly temperature distribution. (b) Matrix temperature distribution. (c) Matrix stress distribution. (d) Matrix displacement distribution. (e) Matrix heat flux distribution. (f) Matrix strain energy density.

temperature field ranging from 951.30 K to 971.72 K, where heat is effectively conducted through the matrix structure from the fuel rods to the adjacent heat pipes, with a smooth temperature variation (Fig. 6(b)). Under the current operating conditions, the overall structure of the HPR matrix exhibits a deformation trend expanding from the center outwards, with a maximum displacement of only 0.0057 mm (Fig. 6(d)).

The stress field shows a maximum stress of 140.72 MPa, concentrated at the edge of the fuel rod hole at the center of the HPR structure, due to compressive stress from fuel rod expansion. The stress at the edges of the structure is lowest, at 36.50 MPa (Fig. 6(c)). The yield stress of 316SS at 1000 K is 100 MPa(refer to the link at the end of the document), indicating that this initial design has already undergone yielding. This phenomenon is common in recent thermal–mechanical coupling analyses of HPRs and remains one of the challenges in current structural design. Optimizing fuel rod placement and power gradient distribution is one effective solution, but this is beyond the scope of this study (Yang et al., 2025; Ma et al., 2021; Jeong et al., 2023). However, recent experiments by Peng et al. on heat transfer from 0 to 1000° demonstrate that, within the small deformation range, although the matrix undergoes local buckling, the maximum Mises stress remains within the ultimate tensile strength range of 380 MPa, and the integrity and functionality of the HPR structure are unaffected (Peng et al., 2025). Therefore, the initial structure of this study is within a safe margin.

It is important to emphasize that Fig. 6(e) and Fig. 6(f) show the heat flux and strain energy density distributions of the matrix, respectively, representing the effective heat transfer path and force transfer path in the structure. In Fig. 6(e), materials between the heat pipe and fuel rod holes contribute the most to heat transfer, while materials between fuel rod holes contribute the least. In Fig. 6(f), materials between fuel rod holes and heat pipe–fuel rod hole interfaces are along the main force transfer paths of the structure. This fundamental reason for the design challenge in HPRs is the trade-off between heat transfer and stiffness objectives, highlighting the necessity of the multi-objective topology optimization method proposed in this study.

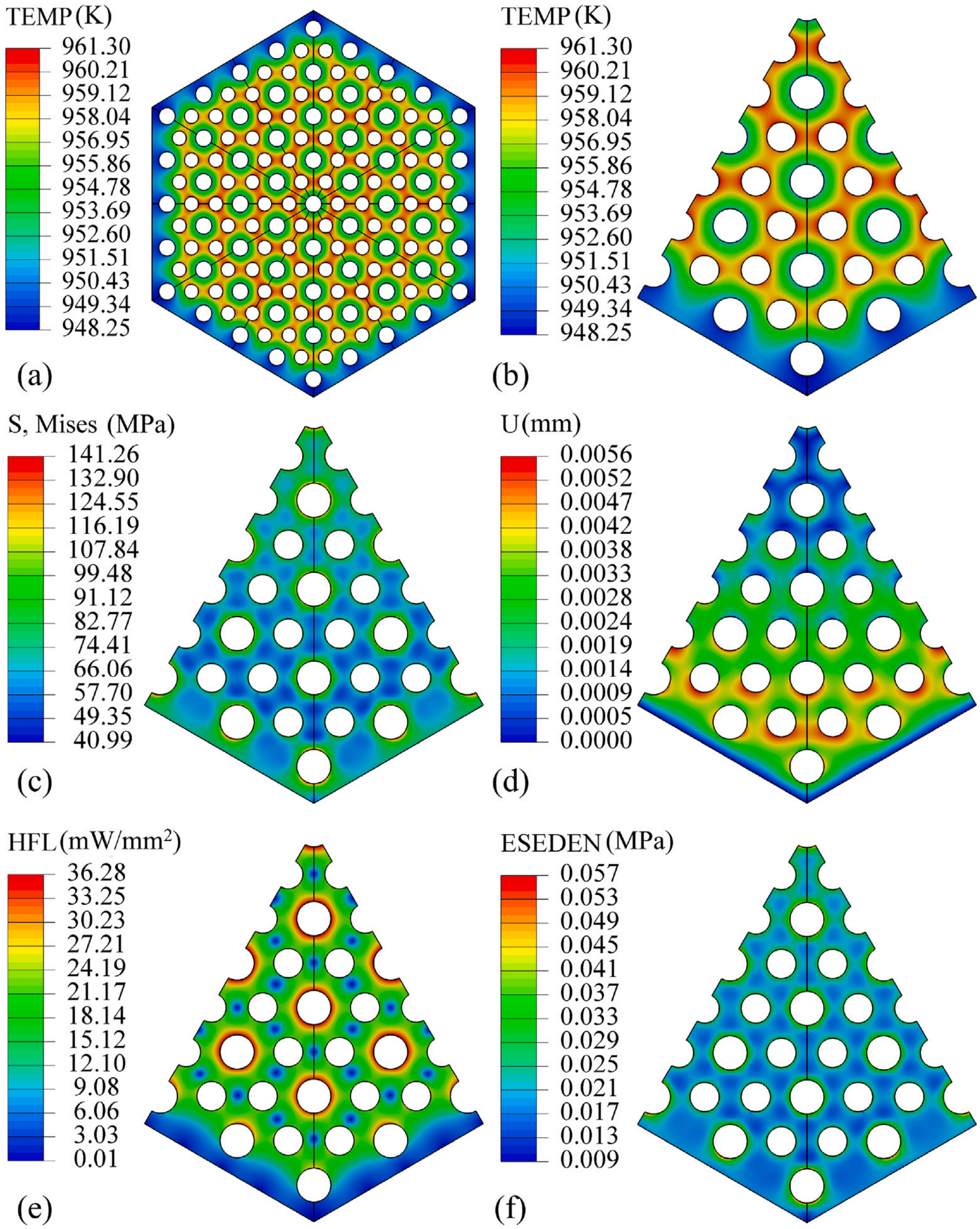

Fig. 7. Thermal–mechanical analysis of the HPR initial design (simplified model): (a) assembly temperature distribution. (b) Matrix temperature distribution. (c) Matrix stress distribution. (d) Matrix displacement distribution. (e) Matrix heat flux distribution. (f) Matrix strain energy density.

Table 2
Error between the initial and simplified FEM models.

Model	$T^{\max}$ (K)	$\sigma^{\max}_{\mathrm{Mises}}$ (MPa)	$U^{\max}$ (mm)	$H^{\max}_{\mathrm{flux}}$ (mW/mm^2)	$E^{\max}_{\mathrm{strain}}$ (MPa)
Initial model	973.17	140.72	0.0057	32.56	0.067
Simplified model	961.30	141.26	0.0056	36.28	0.057
Error	1.22%	0.38%	1.75%	11.43%	14.93%

By comparing the result contour plots of the simplified model (Fig. 7), the full model (Fig. 6) and the maximum value statistics in Table 2, it can be seen that the peak errors in temperature, Mises stress and displacement are only 1.22%, 0.38% and 1.75%, respectively. The peak positions and gradient distributions for temperature and stress coincide closely, while differences in the displacement amplitude distribution appear near the edges of holes in the middle and outer regions of the matrix, although the overall trend remains consistent. By contrast, the maximum values of heat flux and strain energy exhibit larger errors of 11.43% and 14.93%.To further evaluate the potential impact of these numerical errors on the optimization results, we compared the sensitivity distributions and final topological results of the simplified and full models in Fig. 8. As seen in Fig. 8(a) and (c), despite the deviations in absolute values, the normalized sensitivity gradients for both objectives exhibit high similarity. The spatial distributions of low-sensitivity regions (approaching 0, indicating element removal) and high-sensitivity regions (approaching 1, indicating material retention) are consistent between the two models.

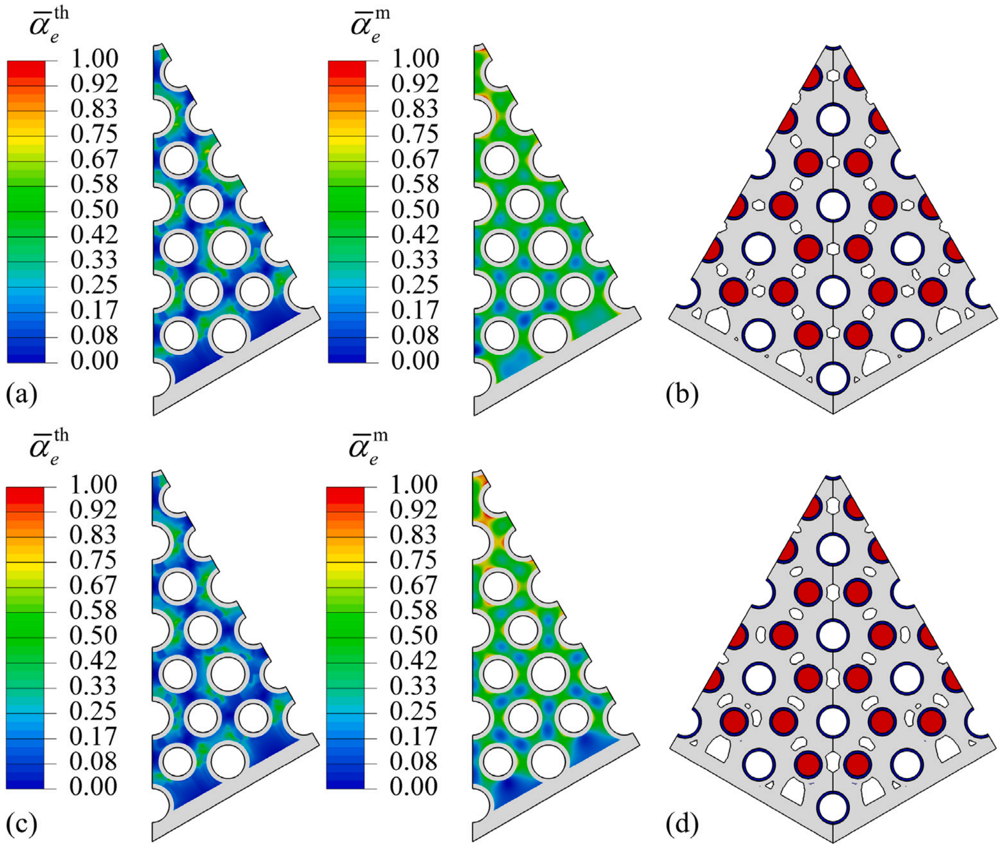

Fig. 8. Comparison of normalized sensitivity distributions and topology optimization results between the simplified model and the full model ($V = 0.8, w_1 = 0.5$): (a) Normalized thermal and mechanical sensitivity distributions of the simplified model. (b) Optimized topology of the simplified model. (c) Normalized thermal and mechanical sensitivity distributions of the full model. (d) Optimized topology of the full model.

Therefore, the final optimized topology generated by the simplified model ($V = 0.8, w_1 = w_2 = 0.5$, Fig. 8(b)) retains the same hole layout and load-bearing paths as the design optimized directly using the full model (Fig. 8(d)), with only minor differences in local hole shapes. Quantitatively, the objective function values optimized based on the full model ($J_{th} = 41226.11\mathrm{W}\cdot\mathrm{K/mm}, J_m = 171.20\mathrm{J}$) are higher than the results of the simplified model ($J_{th} = 35851.32\mathrm{W}\cdot\mathrm{K/mm}, J_m = 148.78\mathrm{J}$). This implies that the Pareto front based on the full model would shift translationally to the upper right in numerical terms, while its shape and the general trend of the scatter distribution would remain unchanged. Although this indicates that the simplified model optimization entails a slight loss in heat transfer efficiency and deformation resistance compared to the full model, rigorous analysis in subsequent sections confirms that these losses do not affect the ultimate effectiveness of the optimization framework presented in this paper. Therefore, the optimization framework based on the simplified model is capable of providing engineeringly reliable optimization guidance while significantly reducing computational costs.

4.2.2. Pareto frontier

Fig. 9 shows the Pareto front obtained through multi-objective topology optimization under volume fraction constraints of 0.6, 0.7, and 0.8. It is evident that the three Pareto fronts are nearly parallel, and as the volume fraction decreases, both mechanical compliance (J_m) and thermal compliance (J_{th}) increase, indicating a trade-off between heat dissipation efficiency and resistance to deformation. Within each Pareto front, a clear trade-off between the two objectives is observed. The endpoints, $w_1 = 0$ and $w_1 = 1$, represent the results of single-objective optimization for heat transfer or stiffness, where the material distribution fully preserves the heat transfer or force transfer path. As the weight factor approaches the middle of the Pareto front, the material distribution gradually converges to a compromise solution for both objectives. When crossing the gray dashed line in the figure (where w_1 is between 0.55 and 0.70), a clear transition in the structural evolution tendency occurs.

Fig. 10 further illustrates the evolution of the maximum Mises stress, temperature, and displacement in the structure for optimization results with different weight distribution ratios. As the structural volume fraction decreases, all three key performance indicators generally increase. Moreover, for each volume fraction constraint, the three key performance indicators exhibit consistent trends based on the weight distribution: when the weight is biased towards minimizing thermal compliance, the maximum temperature decreases, while the maximum Mises stress and maximum displacement increase, reflecting improved heat dissipation efficiency but reduced stiffness. In contrast, when the weight is biased towards minimizing mechanical compliance, the three key performance indicators evolve in the opposite direction. The ultimate tensile strength of 316SS under the temperature conditions in this study is 380 MPa. The proportion of optimization results exceeding this strength in the three Pareto solution sets (with volume fractions of 0.8, 0.7, and 0.6) are 23.8%, 47.6%, and 57.1%, respectively. This indicates that as the structural mass decreases, the risk of matrix fracture failure in the optimized results increases.

4.2.3. Optimal design

The next step is to determine the optimal solution that satisfies the strength constraint from the three Pareto fronts using the ideal point method. Two single-objective optimization results are combined

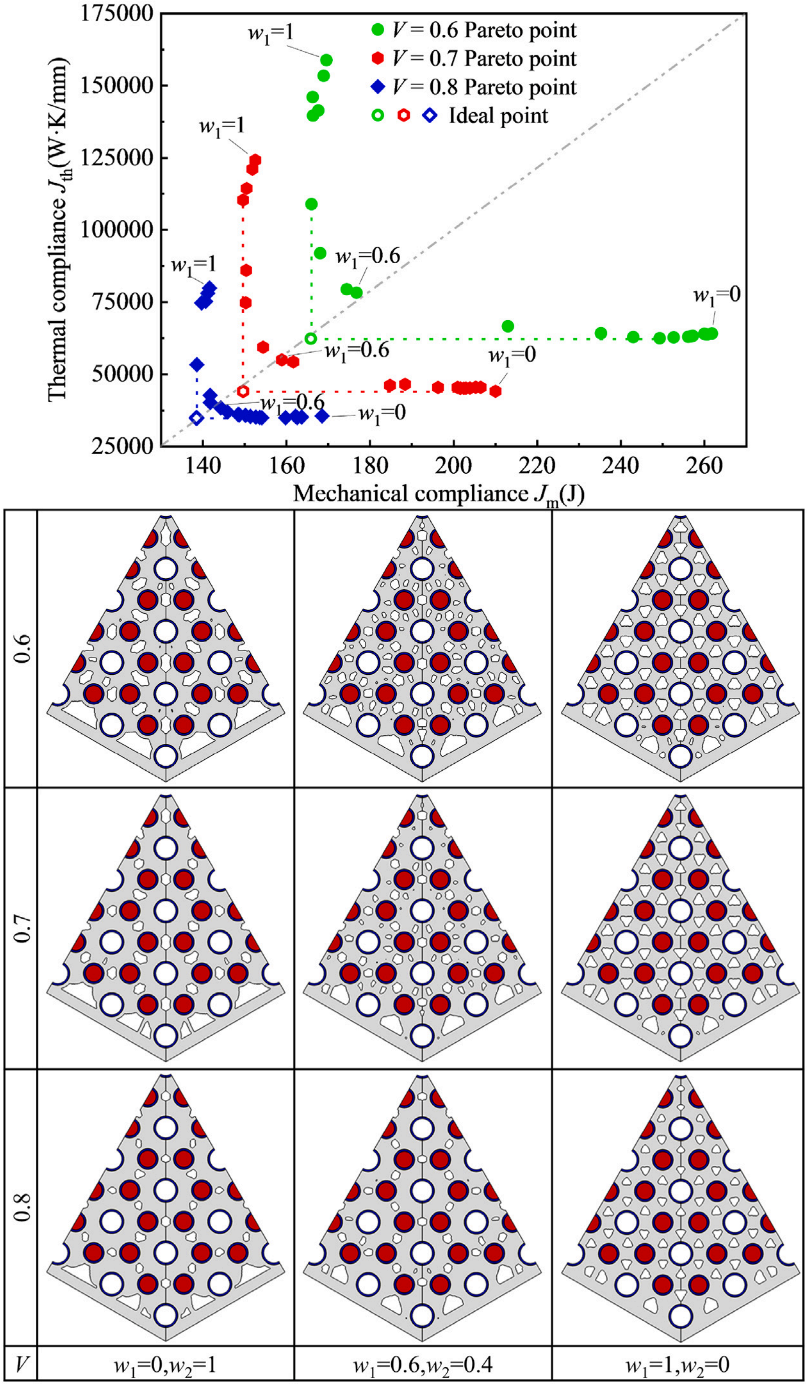

Fig. 9. Pareto front analysis under different volume constraints.

Table 3
Performances of optimal design under different volume fraction constraints.

V	w_1	$J_{th}(w_1)$ (W·K/mm)	$J_m(w_1)$ (mJ)	T^{max} (K)	U^{max} (mm)	σ^{max}_{Mises} (MPa)
0.6	0.6	78174.14	176782.85	974.22	0.0093	238.69
0.7	0.6	54190.95	161699.97	973.17	0.0079	267.38
0.8	0.6	36817.78	145949.87	972.09	0.0089	259.11
1.0	–	24985.40	118084.17	971.72	0.0057	140.72

to form a virtual utopia point $\left(J_m^{min}(w_1), J_{th}^{min}(w_1)\right)$. Then, the non-dominated solution $\left(J_m(w_1), J_{th}(w_1)\right)$ from the Pareto front that has the shortest Euclidean distance to this point is selected as the optimal design. The method is given by the following equation:

$$d(w_1) = \sqrt{\left(J_{th}(w_1) - J_{th}^{min}(w_1)\right)^2 + \left(J_m(w_1) - J_m^{min}(w_1)\right)^2} \qquad (28)$$

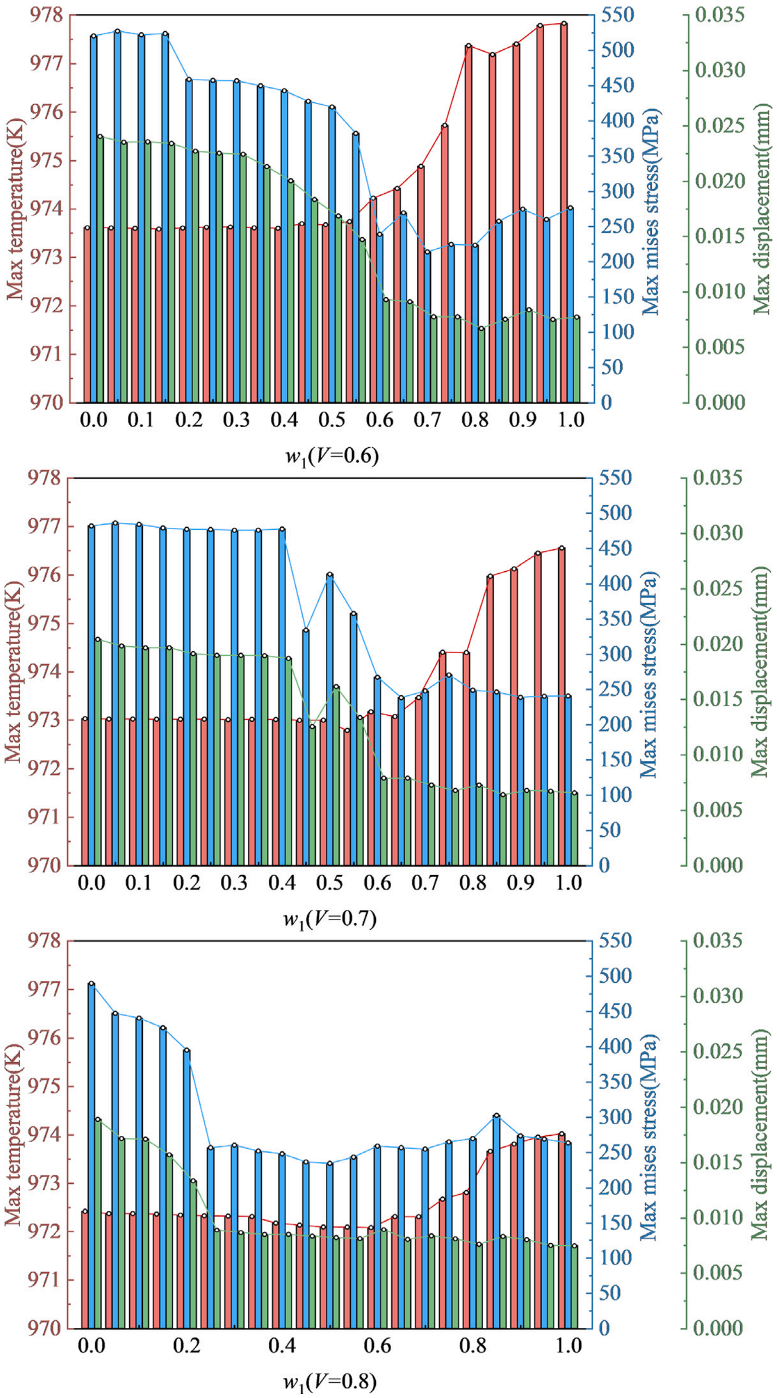

Fig. 10. Performance evolution with varying weight factors of different volume constraints.

Table 3 shows the optimal design solutions for three different volume fraction constraints (V = 0.8, 0.7, and 0.6), all of which meet the ultimate tensile strength requirement. The optimal weight distribution for each design is ($w_1 = 0.6, w_2 = 0.4$), and all solutions are located near the center of the Pareto front shown in Fig. 9 (indicated by the gray dashed line), demonstrating excellent balance. Compared to the initial design, the thermal compliance increased by 32.14%, 53.89%, and 68.04%, while the mechanical compliance increased by 19.09%, 26.97%, and 33.21%. This indicates that lightweighting the structure leads to a decrease in both overall heat dissipation capacity and stiffness. However, further analysis of the corresponding engineering performance indicators shows that the maximum temperature remains stable, with only a 0.25% variation. This suggests that optimizing heat dissipation performance was highly successful. We must carefully consider the trade-off between structural volume fraction and the maximum displacement objective. Therefore, we concluded that V=0.7, w_1=0.6, and w_2=0.4 represent the optimal design for the multiobjective optimization of the HPRs matrix in this study. Compared to the initial design, this trade-off design reduces the structural volume by 30%, with only a 0.15% increase in maximum temperature and a 27.84% increase in maximum displacement.

Fig. 11 illustrates the thermal–mechanical coupled analysis results for the optimal design. Fig. 11(a) presents the temperature distribution of the assembled HPR design and matrix, which follows a pattern

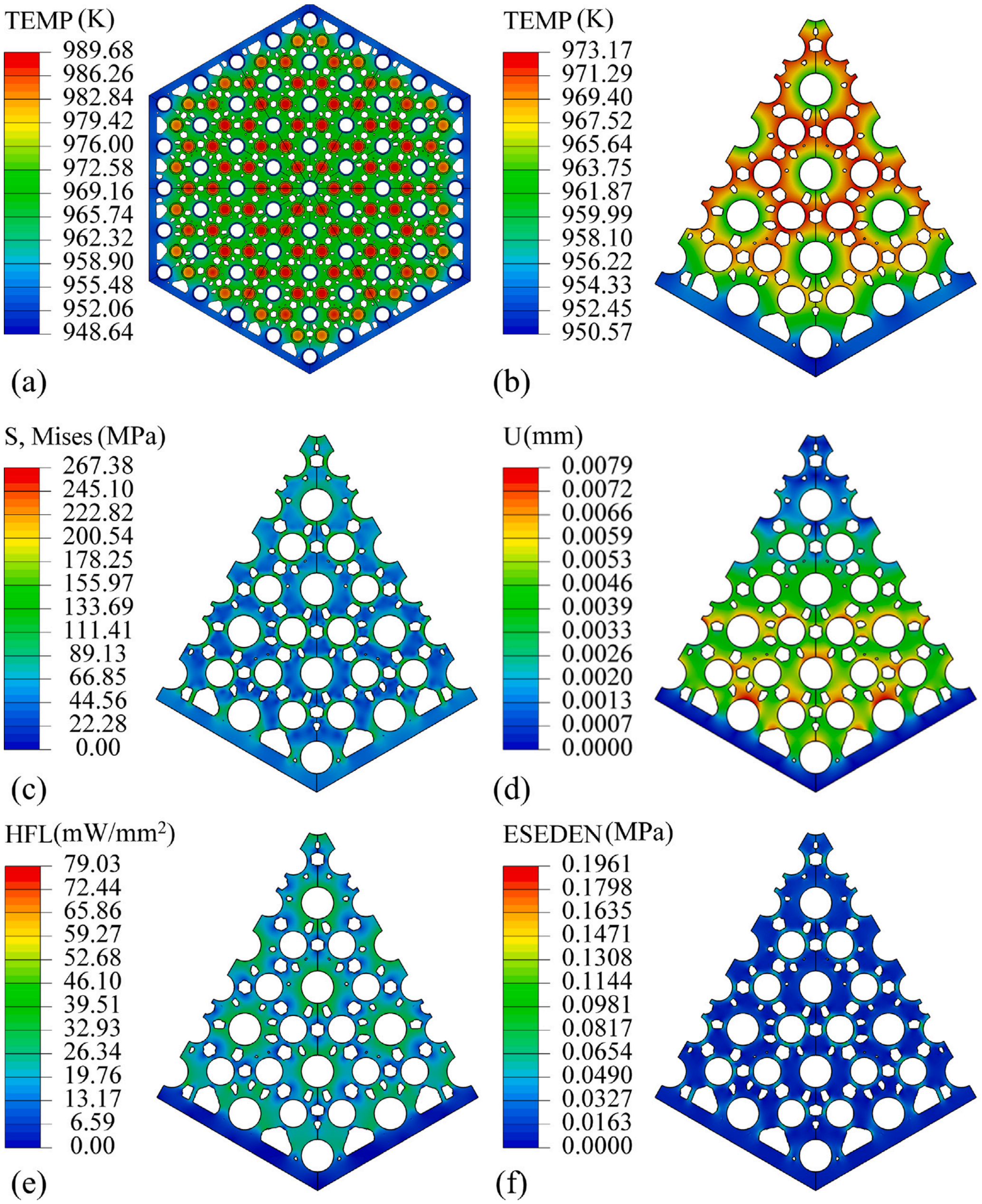

Fig. 11. Thermal–mechanical analysis of the HPR optimized design($V = 0.7$): (a) assembly temperature distribution. (b) Matrix temperature distribution. (c) Matrix stress distribution. (d) Matrix displacement distribution. (e) Matrix heat flux distribution. (f) Matrix strain energy density.

similar to the initial design: heat radiates outward from the center. In the local area, a relatively intact heat transfer path is maintained between the heat pipe and fuel rod, with temperature and heat flow (Fig. 11(e)) evenly distributed along this path. This ensures effective heat dissipation and conduction, demonstrating the success of the multi-objective optimization in enhancing heat dissipation efficiency.

Fig. 11(b) shows the stress field distribution of the optimized design, concentrated near the fuel rod holes, indicating that this region still experiences high local pressure. However, the overall stress distribution is more uniform, with no significant stress concentration. Although the maximum Mises stress has increased, it remains well below the material's ultimate strength. Fig. 11(c) and Fig. 11(e) show displacement and elastic strain energy density distributions that closely resemble those of the initial design, indicating that the optimized design preserves most of the effective force transmission paths. Although the maximum displacement has increased to 0.0079 mm, it remains within the small deformation range, meaning the structure's stiffness has been effectively preserved despite a significant reduction in volume, and is still able to effectively withstand external forces in the operating environment.

Overall, the optimal design exhibits an excellent balance between stiffness and heat dissipation performance in the thermal–mechanical coupled analysis. Despite a significant reduction in structural volume, the heat dissipation performance is strictly maintained. Although the maximum displacement has slightly increased, the structure still exhibits excellent resistance to deformation. This further validates the potential of the proposed optimization method for lightweight design applications in HPRs.

4.2.4. Fatigue life analysis

Since the stress level in the matrix exceeds the yield strength, we perform a thermo-mechanical fatigue analysis of the matrix using the

Fe-safe software to evaluate potential crack initiation sites and service life. By introducing an additional *step* in the finite element model shown in Fig. 4, we fully simulate a complete operating cycle: continuous operation for five years following reactor start-up, followed by shutdown and cooling to ambient temperature. The Fe-safe code reads the `.odb` result file, extracting the total strain information at each element node generated under coupled thermo-mechanical loading. These strain values are then substituted into the left-hand side of the Brown–Miller criterion (Eq. (29)) to calculate fatigue life. This method is commonly used for predicting low-cycle fatigue life of 316SS and has been successfully applied to thermal protection structures of high-temperature reactors (Giannella et al., 2018; Abarkan et al., 2022).

$$\frac{\Delta\gamma_{\max}}{2} + \frac{\Delta\varepsilon_n}{2} = 1.65\frac{\sigma_f'}{E}(2N_f)^b + 1.75\varepsilon_f'(2N_f)^c \tag{29}$$

Here, $\Delta\gamma_{\max}$ denotes the maximum shear strain range; $\Delta\varepsilon_n$ is the strain range normal to the plane of maximum shear strain amplitude; σ_f' is the fatigue strength coefficient; ε_f' is the fatigue ductility coefficient; N_f is the number of cycles to failure; b and c are the fatigue strength and ductility exponents, respectively; and E is Young's modulus. According to the Morrow mean stress correction, σ_f' is replaced by $\sigma_f' - \sigma_m$, where σ_m is the mean stress normal to the critical plane. These parameters are highly temperature-dependent; the Fe-safe database is equipped with detailed parameter values for 316SS over the 20°C–700°C range, and data above 700°C are supplemented by experiments from the Nuclear Power Institute of China. The specific numerical values can be found in the fatigue analysis file linked at the end of the paper.

Fig. 12 presents the fatigue life contour plots (Life-Repeats, where larger values indicate longer life) of the initial design ($V = 1.0$) and the topological designs with different volume fractions under rated power ($10\,\mathrm{mW/mm^3}$) and doubled power ($20\,\mathrm{mW/mm^3}$). Under the rated power, Fig. (a) shows that the minimum fatigue life of the initial design reaches the software display limit of $N_f = 10^7$, which is approximately regarded as no fatigue damage. Fig. (b)–(c) show that as the volume fraction decreases, the fatigue life correspondingly decreases, among which the matrix topology with $V = 0.70$ is relatively optimal, achieving $N_f = 1.70 \times 10^6$. It is evident that in the three volume-fraction topological designs, the cracks associated with longer life always initiate at the edge of internal holes in the matrix, whereas cracks associated with shorter life originate at the edge of the hole containing the fuel rod and propagate to the edge of the internal hole in the matrix. When the fuel rod power increases, the fatigue life of the initial design decreases to 5.47×10^5 — still within the high-cycle fatigue regime — while the life of the $V = 0.70$ topological design sharply decreases to 6.97×10^4, with multiple cracks initiating at the fuel rod hole edge and extending to the nearby hole edge. In summary, under the rated power of $10\,\mathrm{mW/mm^3}$, although the lightweight reinforcement introduced by topological optimization reduces fatigue life, it still ensures safe cyclic operation on the order of several hundred thousand to several million cycles.

4.3. Discussion

It is important to note that strength and fatigue requirements in the current framework are addressed via a posteriori evaluation rather than being formulated in theory. Theoretically, maximizing structural stiffness does not strictly guarantee the minimization of local stress concentrations. Filtering designs through post-optimization verification inherently risks excluding optimal solutions located at the boundaries of the feasible domain, resulting in a contraction of the design space.

While incorporating static stress or fatigue into topology optimization is theoretically mature, several challenges hinder its direct application to the complex HPR model presented here. First, sensitivity analysis for stress constraints necessitates an additional adjoint numerical model and iterative data exchange with the primal model (Takezawa et al., 2014; Kambampati et al., 2020a), leading to computationally prohibitive costs for the nonlinear model in this study. Second, the singularity phenomenon inherent in stress-constrained optimization typically requires delicate tuning of relaxation parameters and aggregation indices, limiting the algorithm's robustness in multi-physics scenarios (Deaton and Grandhi, 2016). Furthermore, fatigue constraints involve history-dependent cumulative damage; decoupling this nonlinear assessment into equivalent static indicators for sensitivity analysis presents extreme mathematical complexity (Holmberg et al., 2014).

However, the proposed multi-objective topology optimization framework, based on the linear aggregation of sensitivity fields, possesses excellent extensibility. This provides a versatile foundation for the future integration of stress and fatigue constraints. Future work will focus on deriving precise sensitivity expressions for these constraints under thermo-mechanical coupling and developing adaptive strategies for numerical singularity control.

The topology optimization employs a 2D generalized plane strain framework, a choice predicated on the HPR core's high aspect-ratio geometry and validated by high-fidelity simulations (Yang et al., 2025) to accurately capture dominant radial heat transfer while reducing the computational burden. However, this approach inherently simplifies 3D effects — such as non-uniform axial expansion caused by cosine power distributions (Sun et al., 2018) or phenomena like pellet hourglassing and core bowing — which cross-sectional models cannot fully capture (Williamson et al., 2012). Regarding 3D extension, the BESO architecture and derived sensitivity analysis (Eqs. 18 and 19) are intrinsically dimension-independent. Specifically, transitioning from 2D quadrilateral to 3D hexahedral elements necessitates only the augmentation of stiffness and thermal conductivity matrices without fundamental alterations to the optimization logic; thus, the proposed framework is theoretically ready for 3D application. Consequently, future work will leverage High-Performance Computers to overcome the associated computational costs to account for these spatial deformation effects.

The matrix structures generated by the proposed multi-objective topology optimization feature intricate, organic geometries, posing significant challenges to conventional subtractive manufacturing techniques such as drilling or milling. However, the rapid advancement of Additive Manufacturing (AM) offers a robust solution for fabricating such complex solid-state cores. In particular, the SS316 matrix material employed in this study exhibits high compatibility with AM processes, as recent studies have validated the performance of AM-fabricated 316SS components in nuclear applications (Peng et al., 2025; Li et al., 2021). Consequently, AM is identified as the primary fabrication route for the optimized HPR matrix. While AM significantly relaxes geometric constraints, practical fabrication must still account for process-specific limitations. Future engineering implementations will therefore apply geometric reconstruction techniques to smooth topology boundaries or directly integrate explicit manufacturing constraints (e.g., draw direction or overhangs) into the optimization algorithm, ensuring printability without compromising performance.

5. Conclusion

This study introduces a thermal–mechanical coupled multi-objective topology optimization framework based on the integration of ABAQUS and BESO. The framework combines the coupling effects of heat transfer and mechanics, thoroughly accounting for complex mechanical behaviors, such as high-temperature creep and gap heat transfer in the solid-state core. This provides an effective solution for optimizing the balance between HPR matrix lightweighting, thermal conduction efficiency, and structural stiffness.

Regarding thermal–mechanical coupled analysis, this study performed secondary development based on ABAQUS to establish a high-fidelity finite element model. This model considers the thermal expansion and creep effects between the heat pipes, fuel rods, their

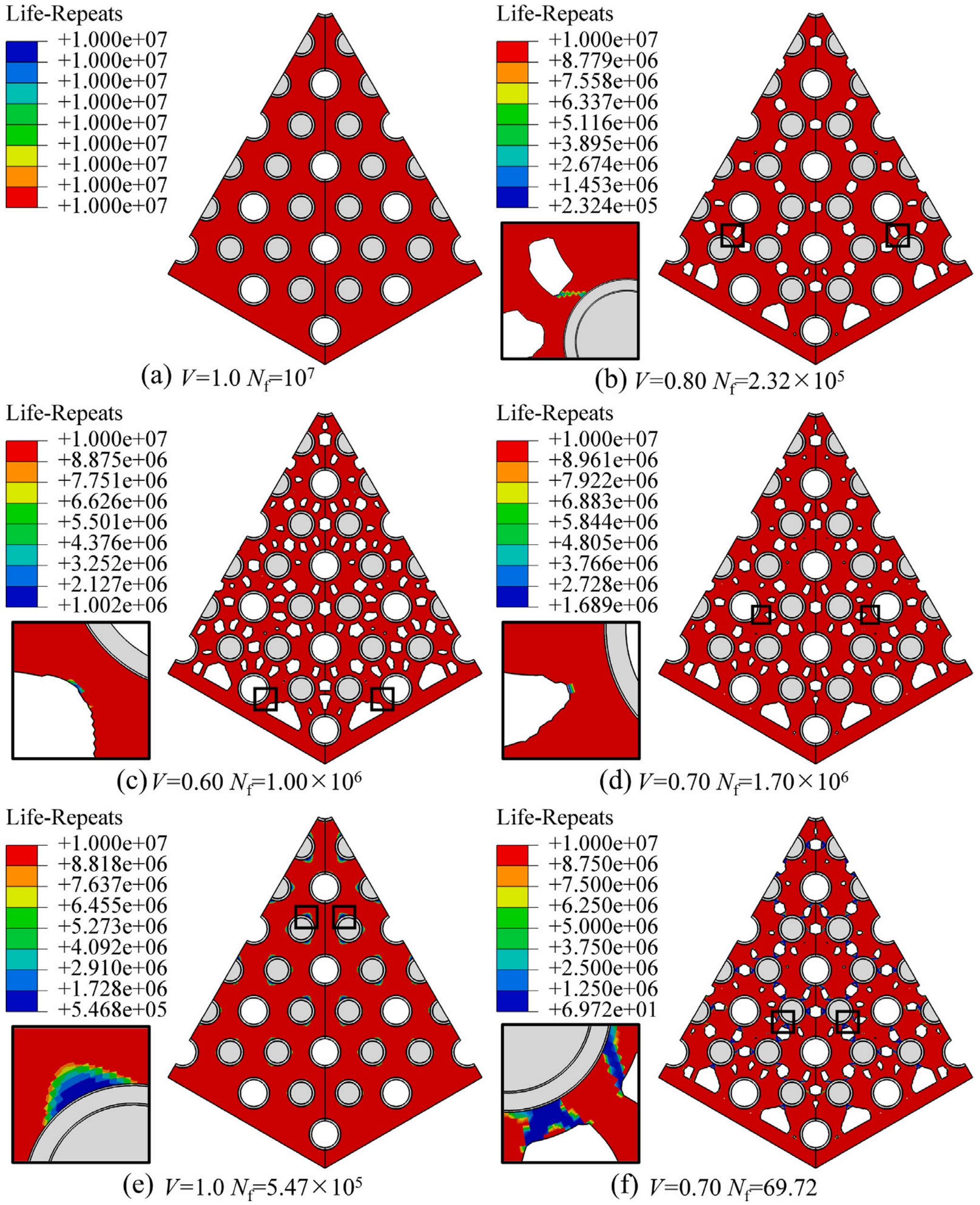

(a) V=1.0 N_f=10^7 (b) V=0.80 N_f=2.32×10^5

(c) V=0.60 N_f=1.00×10^6 (d) V=0.70 N_f=1.70×10^6

(e) V=1.0 N_f=5.47×10^5 (f) V=0.70 N_f=69.72

Fig. 12. Fatigue life contour plots: (a) initial model, $V = 1$, $q = 10\,\mathrm{mW/mm^3}$. (b–d) Topology optimal model, $V = 0.80, 0.60, 0.70$, $q = 10\,\mathrm{mW/mm^3}$. (e) Initial model, $V = 1.0$, $q = 20\,\mathrm{mW/mm^3}$. (f) Topology optimal model, $V = 0.70$, $q = 20\,\mathrm{mW/mm^3}$.

cladding and the matrix, and introduces a refined gap heat transfer modeling approach, enabling accurate assessment of HPR thermal and mechanical performance. In terms of topology optimization, this study proposes a multi-objective topology optimization method based on the BESO theory framework and compromise programming approach. The method minimizes mechanical compliance and thermal compliance, subject to volume fraction constraints. Implemented in the ABAQUS environment, it is easily adaptable to various structural types and complex force-thermal boundary condition optimization problems.

This study provides robust support for reactor structural design and engineering decisions. Specifically, by constructing multi-objective Pareto fronts, the framework offers quantitative trade-off tools for diverse application scenarios. This enables designers to make precise decisions balancing structural stiffness and heat dissipation efficiency according to specific mission requirements—ranging from mass-sensitive deep space exploration and high-reliability deep-sea submersion to land-based mobile transport scenarios where both structural safety and thermal efficiency are critical. Furthermore, the stress concentration evolution laws and fatigue crack initiation mechanisms identified by the optimization framework (e.g., the tendency for cracks to propagate from the fuel hole edge towards the matrix thin walls) provide a direct geometric basis for the local reinforcement design of critical regions in the solid-state matrix. The validated simplified equivalent analysis method significantly reduces computational costs while ensuring accuracy, effectively supporting large-scale scheme screening during the preliminary engineering design phase. Meanwhile, the fatigue life prediction data serves as an important engineering reference for determining reactor maintenance cycles and service life limits.

While the thermal–mechanical coupling and topology optimization methods applied in this study have achieved initial success in HPR matrix design, there is still potential for further optimization, particularly regarding the high stress levels in the matrix, which remain above the yield strength. Future research will focus on advancing multi-material continuum topology optimization theories and joint optimization methods based on fuel rod layouts, power gradients, and matrix topology, to further enhance the lightweight design, long-term stability, and multi-condition adaptability of HPRs.

CRediT authorship contribution statement

Hao Jin: Writing – original draft. **Mingkai Yue:** Validation, Methodology. **Di Yun:** Supervision. **Jinxiong Zhou:** Writing – review & editing.

Data, materials, and software availability

Relevant files and data are provided on GitHub (https://github.com/jinhao-ok1/thermal-mechanic-topology-optimization-.git), including the Abaqus-based Python program for thermal–mechanical coupled topology optimization, temperature-dependent material property tables for 316SS and UO2, UMAT subroutine files, and the Abaqus input file for the solid-state core thermal–mechanical coupled analysis.

Declaration of competing interest

The authors declare that they have no known competing financial interests or personal relationships that could have appeared to influence the work reported in this paper.

Acknowledgment

This research is supported by the National Natural Science Foundation of China (grant U23B2071).

Data availability

I have shared the data and code at the link provided at the end of the manuscript.

References

Abarkan, I., Shamass, R., Achegaf, Z., Khamlichi, A., 2022. Numerical and analytical studies of low cycle fatigue behavior of 316 LN austenitic stainless steel. J. Press. Vessel. Technol. 144 (6), 061507.

Ali, M.A., Shimoda, M., 2022. Toward multiphysics multiscale concurrent topology optimization for lightweight structures with high heat conductivity and high stiffness using MATLAB. Struct. Multidiscip. Optim. 65, 207.

Cao, H., Wang, G., 2019. The research on the heat transfer of a solid-core nuclear reactor cooled by heat pipe through a numerical simulation, considering the assembly gaps. Ann. Nucl. Energy 130, 431–439.

Deaton, J.D., Grandhi, R.V., 2016. Stress-based design of thermal structures via topology optimization. Struct. Multidiscip. Optim. 53 (2), 253–270.

El-Genk, M.S., Schriener, T.M., 2025. Lightweight heat pipe radiator for nuclear reactor power systems on lunar surface. Nucl. Technol. 211, 400–428.

Gaffard, V., Besson, J., Gourgues-Lorenzon, A.-F., 2005. Creep failure model of a tempered martensitic stainless steel integrating multiple deformation and damage mechanisms. Int. J. Fract. 133, 139–166.

Giannella, V., Citarella, R., Fellinger, J., Esposito, R., 2018. LCF assessment on heat shield components of nuclear fusion experiment "wendelstein 7-X" by critical plane criteria. Procedia Struct. Integr. 8, 318–331.

Gilbert, E.R., Garner, F.A., 2007. The influence of cold-work level on the irradiation creep and swelling of AISI 316 stainless steel irradiated as pressurized tubes in the EBR-II fast reactor. J. Nucl. Mater. 367, 954–959.

Guanghui, S., Chengqi, G., Dongliang, Q., Dongtao, W., Lei, T., Tong, G., 2020. An aerospace bracket designed by thermo-elastic topology optimization and manufactured by additive manufacturing. Chin. J. Aeronaut. 33, 1252–1259.

Hao, J., Ning, A., Qilong, J., Chun, S., Xiaofei, M., Jinxiong, Z., 2025. Multi-objective topology optimization for cutout design in deployable composite thin-walled structures. Chin. J. Aeronaut. 103530.

He, D., Liu, S., 2008. BESO method for topology optimization of structures with high efficiency of heat dissipation. Int. J. Simul. Multidiscip. Des. Optim. 2, 43–48.

Holmberg, E., Torstenfelt, B., Klarbring, A., 2014. Fatigue constrained topology optimization. Struct. Multidiscip. Optim. 50 (2), 207–219.

Holmström, S., Pohja, R., Nurmela, A., Moilanen, P., Auerkari, P., 2013. Creep and creep-fatigue behaviour of 316 stainless steel. Procedia Eng. 55, 160–164.

Huang, D., Zhou, S., Yan, X., 2025. Multi-objective optimization design of power pack structures based on floating projection topology optimization. Eng. Optim. 57, 361–383.

Jeong, M.J., Im, J., Lee, S., Cho, H.K., 2023. Multiphysics analysis of heat pipe cooled microreactor core with adjusted heat sink temperature for thermal stress reduction using openfoam coupled with neutronics and heat pipe code. Front. Energy Res. 11, 1213000.

Kambampati, S., Gray, J.S., Kim, H.A., 2020a. Level set topology optimization of structures under stress and temperature constraints. Comput. Struct. 235, 106265.

Kauzmann, W., 2012. Kinetic Theory of Gases. Courier Corporation.

Li, H., Yue, T., Zhu, F., Peng, Y., Li, Y., Huang, C., Zhang, Y., 2021. Research on application of additive manufacturing technology in nuclear fuel assembly field. In: International Conference on Nuclear Engineering, vol. 85253, American Society of Mechanical Engineers, V002T05A017.

Ling, S., Li, W., Zheng, L., Wan, C., Liu, Y., 2023. Multidisciplinary collaborative topology optimization method for perforated plates. Eng. Struct. 297, 116924.

Liu, Y.-C., Liu, Y.-L., Zhao, Y., Liu, Z., Zhou, T., Zou, Q., Zeng, X., Zhong, Y.-K., Li, M., Sun, Z.-x., et al., 2020. A simple and effective separation of UO2 and Ln2O3 assisted by NH4Cl in LiCl–KCl eutectic. J. Nucl. Mater. 532, 152049.

Liu, R., Prudil, A., Zhou, W., Chan, P.K., 2016. Multiphysics coupled modeling of light water reactor fuel performance. Prog. Nucl. Energy 91, 38–48.

Liu, Z., Xu, X., Wu, H., Cao, L., 2021. Multidimensional multiphysics simulations of the supercritical water-cooled fuel rod behaviors based on a new fuel performance code developed on the MOOSE platform. Nucl. Eng. Des. 375, 111085.

Luo, W., Guo, X., Dai, J., Rao, T., 2021. Hull optimization of an underwater vehicle based on dynamic surrogate model. Ocean Eng. 230, 109050.

Ma, Y., Liu, M., Xie, B., Han, W., Yu, H., Huang, S., Chai, X., Liu, Y., Zhang, Z., 2021. Neutronic and thermal-mechanical coupling analyses in a solid-state reactor using Monte Carlo and finite element methods. Ann. Nucl. Energy 151, 107923.

Macdonald, P.E., Thompson, L.B., 1976. MATPRO: a handbook of materials properties for use in the analysis of light water reactor fuel rod behavior. Specif. Nucl. React. Assoc. Plants.

Mao, Z., Yan, S., 2018. Design and analysis of the thermal-stress coupled topology optimization of the battery rack in an AUV. Ocean Eng. 148, 401–411.

Peng, X., Liu, C., Deng, Y., Nie, J., Wu, Y., Su, G., 2025. Research on thermo-mechanical response of solid-state core matrix in a heat pipe cooled reactor. Energies 18, 1423.

Poston, D.I., Gibson, M.A., Godfroy, T., McClure, P.R., 2020. KRUSTY reactor design. Nucl. Technol. 206, 13–30.

Sun, H., Ma, P., Liu, X., Tian, W., Qiu, S., Su, G., et al., 2018. Conceptual design and analysis of a multipurpose micro nuclear reactor power source. Ann. Nucl. Energy 121, 118–127.

Sun, H., Tang, S., Wang, C., Zhang, J., Zhang, D., Tian, W., Qiu, S., Su, G., 2020. Numerical simulation of a small high-temperature heat pipe cooled reactor with CFD methodology. Nucl. Eng. Des. 370, 110907.

Takezawa, A., Yoon, G.H., Jeong, S.H., Kobashi, M., Kitamura, M., 2014. Structural topology optimization with strength and heat conduction constraints. Comput. Methods Appl. Mech. Engrg. 276, 341–361.

Van Uffelen, P., Hales, J., Li, W., Rossiter, G., Williamson, R., 2019. A review of fuel performance modelling. J. Nucl. Mater. 516, 373–412.

Was, G., Petti, D., Ukai, S., Zinkle, S., 2019. Materials for future nuclear energy systems. J. Nucl. Mater. 527, 151837.

Williamson, R., 2011. Enhancing the ABAQUS thermomechanics code to simulate multipellet steady and transient LWR fuel rod behavior. J. Nucl. Mater. 415, 74–83.

Williamson, R.L., Hales, J., Novascone, S., Tonks, M., Gaston, D., Permann, C., Andrs, D., Martineau, R., 2012. Multidimensional multiphysics simulation of nuclear fuel behavior. J. Nucl. Mater. 423 (1–3), 149–163.

Yan, B.H., Wang, C., Li, L.G., 2020. The technology of micro heat pipe cooled reactor: A review. Ann. Nucl. Energy 135, 106948.

Yang, X., Li, Q., Zhang, J., Wu, Y., He, Y., Li, C., Wang, M., Guo, K., Wang, C., Su, G., et al., 2025. Thermal-mechanical coupling behavior analysis of solid-state constrained component in advanced nuclear energy system. Energy 136779.

Yvon, P., Carré, F., 2009. Structural materials challenges for advanced reactor systems. J. Nucl. Mater. 385, 217–222.

Zhang, Y., Li, R., Zhang, X., Tao, Z., Xia, G., Du, X., 2024. Lightweight optimization of space reactor loop heat pipe radiation radiator based on surrogate models. Prog. Nucl. Energy 170, 105158.

Zhang, W., Zhang, D., Wang, C., Tian, W., Qiu, S., Su, G., 2020. Conceptual design and analysis of a megawatt power level heat pipe cooled space reactor power system. Ann. Nucl. Energy 144, 107576.

Zuo, Z.H., Xie, Y.M., 2015. A simple and compact python code for complex 3D topology optimization. Adv. Eng. Softw. 85, 1–11.